Tombo Propeller: Bioinspired Deformable Structure Toward Collision-Accommodated Control for Drones

Son Tien Bui, *Student Member, IEEE*, Quan Khanh Luu, *Student Member, IEEE*, Dinh Quang Nguyen, *Member, IEEE*, Nhat Dinh Minh Le, Giuseppe Loianno, *Member, IEEE*, and Van Anh Ho, *Senior Member, IEEE*

***Abstract*—There is a growing need for vertical takeoff and landing vehicles, including drones, which are safe to use and can adapt to collisions. The risks of damage by collision, to humans, obstacles in the environment, and drones themselves, are significant. This has prompted a search into nature for a highly resilient structure that can inform a design of propellers to reduce those risks and enhance safety. Inspired by the flexibility and resilience of dragonfly wings, we propose a novel design for a biomimetic drone propeller called Tombo propeller. Here, we report on the design and fabrication process of this biomimetic propeller that can accommodate collisions and recover quickly, while maintaining sufficient thrust force to hover and fly. We describe the development of an aerodynamic model and experiments conducted to investigate performance characteristics for various configurations of the propeller morphology and related properties, such as generated thrust force, thrust force deviation, collision force, recovery time, lift-to-drag ratio, and noise. Finally, we design and showcase a control strategy for a drone equipped with Tombo propellers that collides in midair with an obstacle and recovers from collision continuing flying. The results show that the maximum collision force generated by the proposed Tombo propeller is less than two-thirds that of a traditional rigid propeller, which suggests the concrete possibility to employ deformable propellers for drones flying in a cluttered environment. This research can contribute to the morphological design of flying vehicles for agile and resilient performance.**

***Index Terms*—Biomimetic design, collision accommodated, deformable propeller, drones' safety, soft robotics.**

Manuscript received 30 January 2022; revised 3 June 2022; accepted 8 August 2022. Date of publication 26 August 2022; date of current version 8 February 2023. This article was recommended for publication by Associate Editor Hector Garcia de Marina and Editor Paolo Robuffo Giordano upon evaluation of the reviewers' comments. This work was supported in part by JST SCORE under Project STSC200006, in part by the Grant-in-aid for Scientific Research KAKENHI under Grant 18H01406 and Grant 21H01287, and in part by AOARD Basic Research Grant under Award FA2386-22-1-4033. *(Corresponding author: Van Anh Ho.)*

Son Tien Bui, Quan Khanh Luu, and Nhat Dinh Minh Le are with the Soft Haptics Laboratory, School of Materials Science, Japan Advanced Institute of Science and Technology, Nomi 923-1292, Japan (e-mail: son-bui@jaist.ac.jp; quan-luu@jaist.ac.jp; nhat-le@jaist.ac.jp).

Dinh Quang Nguyen is with the Soft Haptics Laboratory, School of Materials Science, Japan Advanced Institute of Science and Technology, Nomi 923-1292, Japan, and also with the Institute of Technology, Hanoi University of Industry, Hanoi 11915, Vietnam (e-mail: dinh-nguyen@haui.edu.vn).

Giuseppe Loianno is with the Tandon School of Engineering, New York University, Brooklyn, NY 11201 USA (e-mail: loiannog@nyu.edu).

Van Anh Ho is with the Soft Haptics Laboratory, School of Materials Science, Japan Advanced Institute of Science and Technology, Nomi 923-1292, Japan-PRESTO, Japan Science and Technology Agency, Kawaguchi 332-0012, Japan (e-mail: van-ho@jaist.ac.jp).

This article has supplementary material provided by the authors and color versions of one or more figures available at https://doi.org/10.1109/TRO.2022.3198494.

Digital Object Identifier 10.1109/TRO.2022.3198494

I. Introduction

DRONES, such as popular vertical takeoff and landing, have brought enormous benefits to humans operating in various sectors, such as providing surveillance service, including monitoring, inspection, logistics, transportation, and entertainment. Owing to their compact dimension and flight agility in small spaces, drones attract interest from both the academia and the industry with the potential of large market [1], [2]. Several projects were launched to elaborate the potentials of drones in industry, such as Prime Air (Amazon—2013), Wing (Alphabet—2014), and DRONES (FedEx—2018) for autonomous drone delivery service, FarmBeats (Microsoft in partnership with DJI—2015) for enabling data-driven farming, Aquila (Facebook—2014) for solar-powered drone as an atmospheric satellite, and Skylink (IBM—2016) for remote control aircraft. One of the primary concerns in the operation of drones is the risk of injury to humans or damage to property—both objects in the environment and the drone itself—which may occur during flight or in the event of a collision. In such a scenario, a drone could seriously harm a human or significantly damage something and drop and crash due to damaged propellers. With that in mind, many technologies promoting the safety of drones have been introduced, such as safety cages for drones (hardware) and vision-based obstacle-avoiding algorithms (intelligence). While the former increases the size and physical load of a drone, the latter increases the computational load on its central processor, resulting in the tradeoff of high efficiency costs for safety. Nevertheless, the desire to operate drones in cluttered environments or nearby humans is growing and necessitates strategies to mitigate injuries or damages caused by unexpected collisions.

Meanwhile, in the natural world, flying insects, such as dragonfly [3], yellowjacket, and bumblebee [4], seem to effortlessly accommodate collisions with objects in their surroundings without leaving any footprint of damage [5], [6]. In fact, mother nature is the greatest creator, and at the same time, she is a living encyclopedia from which robotics researchers may learn invaluable knowledge and glean hints for solving engineering problems. In this article, the dragonfly wing construction is an excellent example of shock absorption and self-recovery due to the high flexibility of a hinge-like structure called *nodus* [3]. From the perspective of soft robotics, biomimicry of such structures or functions is a key to solve the safety problem of drones.

This article presents the Tombo propeller. Without requiring the burden of a heavy physical or computational load, toward

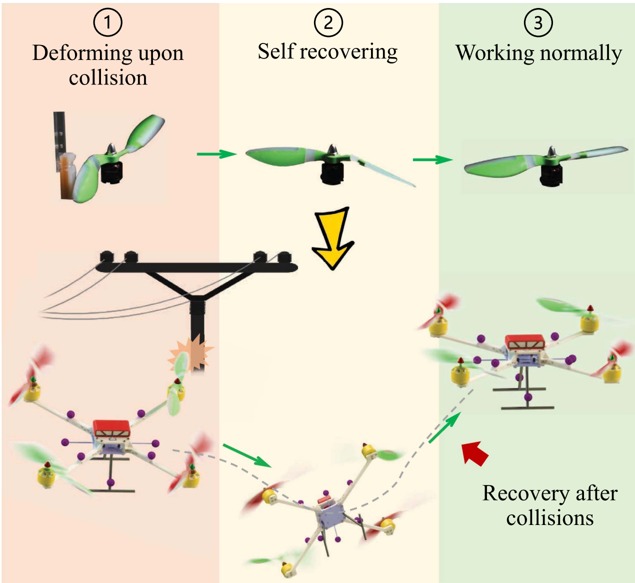

Fig. 1. Safety drone equipped with Tombo propellers. Collision-accommodated propellers that can deform passively upon collision then self-recover to work normally are employed for uncrashed drones.

ultimate safety for drones, this biomimetic design deformable propeller can accommodate collisions while retaining sufficient rotation thrust to remain airborne, as shown in Fig. 1. The key structure of the Tombo propeller is its hinge-like *nodus*, which is a deformable joint made of silicone and fiber tendons [see Fig. 2(a)] bioinspired by the function and structure of the dragonfly wing nodus. Owing to the *nodus* mechanism, a Tombo propeller can self-recover and rotate properly within an average of 0.46 s at the rotational speed of 2000 r/min upon collision, enabling the promising recovery of drones after sudden collisions with their surroundings. The flying and collision experiment of drone with Tombo propellers proved that such recovery time is sufficient for a drone to recover after colliding at 2-m height. In addition, the hybrid design made of soft and hard parts enables the propeller to regain stiffness and generate sufficient rotation thrust to fly the drone. Moreover, with its deformable leading edge, the Tombo propeller imparts lower impact force and damage upon collision with an object than that by a traditional drone propeller, thus further improving the safety of the propeller and struck object. The main contributions of this research are as follows:

1) proposal of a novel biomimetic design for drone propellers;
2) construction of an aerodynamic model of the Tombo propeller and an open-source program for aerodynamic parameter simulation;[1]
3) theoretical and experimental characterization of the Tombo propeller with different configurations of *nodus*;
4) proposal of a control strategy, which includes collision recovery by a drone with Tombo propellers.

[1][Online]. Available: https://github.com/Ho-lab-jaist/tombo-propeller.git

Compared with our previous paper [7], where we only introduced the design, fabrication, and preliminary measurement of thrust force of the Tombo propeller; in this article, we present a thorough analysis and evaluation of the propeller considering variations in its material's composition and configuration as well as different rotational speeds. In addition, we propose a model for the characterization of generated thrust force, taking into account the deformation of the Tombo propeller and its aerodynamic properties. We propose several metrics to evaluate and identify the optimal design according to the user needs. Finally, we also test the flight ability of real drone platform using the Tombo propeller and propose a simplified control strategy for showing the feasibility of the recovery of drone after the collision.

In this article, a concrete review of drones and related work is mentioned in Section II, followed by the biomimetic design of a 9-in (228.6 mm) long Tombo propeller in Section III. Section IV briefly introduces a derivation of an aerodynamic model for the Tombo propeller. Section V provides the details of Tombo propeller characteristic measurement experiments, which is followed by the results in Section VI. Next, Section VII presents a control strategy and showcases the flying of an embedded Tombo propeller drone. Then, the discussion is given in Section VIII. Finally, Section IX concludes this article.

II. Related Works

In this section, we focus on solutions that have been introduced to improve the safety of drones and unmanned aerial vehicles (UAVs). Overall, these solutions can be classified into two groups: *collision avoidance* and *collision impact reduction*. Details can be found in the following.

For collision avoidance, the following approaches have been proposed: geometric, force field, optimized, sense, and avoid [8], [9]. Here, passive sensors (monocular camera [10] and depth camera [11]), active sensors (ultrasonic sensor [12], light detection and ranging [13], and radar [14]), or a combination of them [15], [16] are preferable to detect objects within the flying range. Although such cameras have a large field of view and high resolution, their associated obstacle detection algorithm is greatly affected by weather conditions, lighting, and shiny or reflective surfaces. In addition, vision sensors work best with stationary subjects; yet, they are required to passively respond to high-speed moving images exceeding 35 km/h [17] and are limited at blind spots. Moreover, sensors are needed to overcome the blind spot factor and improve the accuracy of calculation, resulting in increased weight and higher cost UAVs. Recently, event cameras have been applied to UAVs with promising results in terms of avoiding fast-moving obstacles [18]. However, the event camera has a heavier weight, larger size, and higher noise than those of a standard one at the same resolution. Furthermore, the high noise of an event camera reduces its accuracy at large distances, limiting the reliable detection range to 1.5 m.

Regarding collision impact reduction, solutions to protect the actuators (rotors) from collisions or facilitate recovery after a collision require additional features. In most cases, a cage [19],

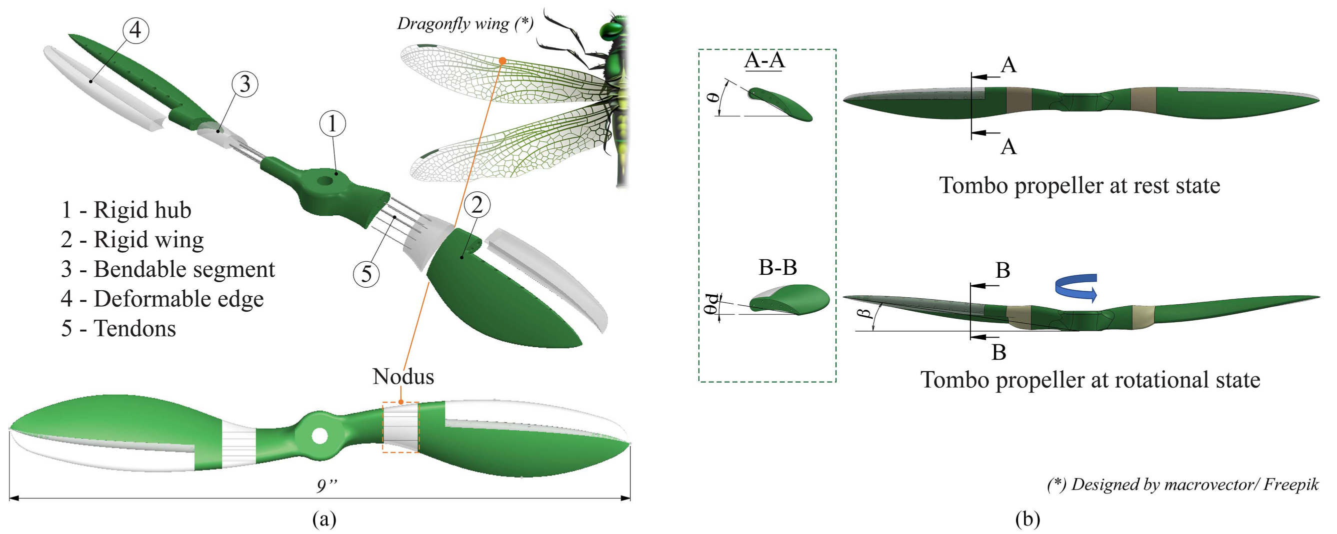

Fig. 2. Tombo propeller anatomy. (a) Design of a Tombo propeller includes a rigid hub, two wings, two soft blades, and two *nodus* with tendons inside. (b) Effect of the deformable *nodus* on the geometrical parameters of the propeller results in decreasing thrust generation. In return, owing to *nodus* flexibility, the Tombo propeller can self-recover and work normally upon collision. (a) Design of a Tombo propeller inspired by a dragonfly wing. (b) Effect of deformable *Nodus* on geometrical characteristics of the Tombo propeller at working states.

[20], [21], [22] is employed due to low cost, low profile, and simple setup; for instance, protective cages shielding motors and preventing multidirectional concurrences. However, their bulky structure may inversely bring a higher risk of collision, and they greatly increase the drone weight, thus reducing the flight time. As an alternative approach, foldable structures [23], [24] could help UAVs decrease their dimension and risk of crashing, especially when flying through a narrow gap. Another exciting approach combines rigid guards and soft deformable mechanisms to reduce crash impact, absorb collision shock, and retain resilience [25], [26], [27], [28]. However, such integration may require a complex control strategy and high resource consumption in practical scenarios. Foldable propellers [29], [30] can accommodate collision and recover in the folding plane thanks to the rotating joints and the centrifugal force, respectively. However, they cannot prevent the collision from other directions, such as parallel with the rotor axis in the case of Aero-Naut CAM carbon folding propeller [30]. In addition, the recovery process after the in-air collision strongly depends on the centrifugal force, which means that the recovery time may take longer than the essential time for the recovery control of the drone. Recently, the notion of a flexible blade [31] has gained attention since this structure may enable propellers to deform and recover upon collision without any additional mechanism. Nonetheless, a flexible blade remains dangerous for soft objects, such as human skin. Furthermore, large-sized thin blades experience great deformation during rotation, limiting the use of these propellers in large UAVs.

Consequently, a tradeoff between the safety of UAVs and their structure and configuration exists. Therefore, despite efforts to improve the structure, integrate perception, and avoid collisions, drones and UAVs remain vulnerable to collisions because of the technical limitations of sensors and unpredictable factors. This poses a great challenge, as nowadays, UAVs are becoming increasingly popular and being used for more application in complex, cluttered, or partially known environments. Hence, there remains a big question: is there a solution that significantly improves the safety of drones but does not largely compromise their basic design and function?

III. Biomimetic Design

Insect wings often suffer stress due to wind gusts and collisions with the surroundings [4]. Therefore, the insect wings evolved to adopt an antishock or shock-absorption structure, resulting in the mitigation of wing damage upon collision [5], [6]. Regarding the dragonfly wing structure, one of the most important parts is the *nodus*, which has a one-way hinge-like structure that can passively flex upon external contact [3]. This part allows the wing to twist, bend, or even fold without incurring damage that foldable propellers cannot manage. The natural *nodus* containing resilin (similar to isotropic rubber) can provide both structural reinforcement and shock absorption. These characteristics provide a hybrid structure (stiff and flexible) that both ensure aerodynamic properties when flying and reduce the risk of damage to the wing upon collision. Based on the characteristics of the dragonfly wing nodus, we propose a novel deformable propeller, which we named Tombo propeller [Fig. 2(a)]. The rigid parts include a hub 1 and wing 2, connected by a nodus-like bendable segment 3 made from silicon rubber and reinforced by embedded tendons 5, nylon fibers) that connect rigid parts (hub and wings). The fibers were distributed to satisfy equal distances among them within the cross section toward the homogeneity of the *nodus*' materials and the ease of drilling holes for the fiber insertion. A deformable edge 4 can be added for the rapid absorption of an impact at the time of collision.

An available slow-flyer propeller model [32] was considered as a reference for the development of the Tombo propeller.

Based on this reference propeller, we used thick airfoils to design a suitable morphology for the propeller. These airfoils not only assure a relatively stiff structure for stable working (with small deformation and vibration), but also accommodate fiber placements inside the *nodus*. In detail, the airfoil along the span length can be extracted by *AirfoilGenerator*—an airfoil tool that we developed for detecting any airfoil from an arbitrary propeller's 3-D model (see the code and implementation in our Git project[2]).

In our initial work [7], the rigid parts of the propellers were made of acrylonitrile butadiene styrene (ABS) using fused-filament-fabrication-based 3-D printing that creates a layered structure, which eventually reduces the strength among layers upon lateral impact. Therefore, in this article, we propose a novel generation model; the rigid parts are fabricated by injection molding as commercial rigid propellers to enhance the uniform of the Tombo propeller. To enhance the propeller surface quality, especially the *nodus*-like part, molds were made of aluminum alloy fabricated by machining instead of ABS fabricated by 3-D printing. The fabrication process for a Tombo propeller has been described [7].

Nodus mechanical property and performance strongly affects the working ability of the proposed propeller. As illustrated in Fig. 2, when the propeller rotates, there is a decrease in pitch angle θ, which is due to the inherent propeller's deformation. This negatively affects thrust force generation since it depends largely on the pitch angle. In addition, the softness of the *nodus* may influence the working stability of a drone equipped with Tombo propellers. Therefore, in this research, we investigate various configurations of the *nodus* structure and materials (silicone rubber embedded with monofilament nylon fibers), i.e., the morphology, to determine an optimum construction of the Tombo propeller.

IV. Aerodynamic Model of the Tombo Propeller

Previous research has indicated that aerodynamic parameters, such as drag and thrust forces [33], [34], [35], blade flapping [34], [36], and so on, strongly affect the flight characteristics of drones. Control approaches for drones require consideration to aerodynamic parameters to attain stability during dynamic flight or hovering [37]. Therefore, in developing an aerodynamic model of the Tombo propeller, mechanical properties play an important role for its application to standard UAVs.

A. Revisit of the Aerodynamic Model of a Classical Propeller

Aerodynamic models of standard propellers and quadrotors have been established and well developed [38], [39], [40]. The most important factors of aerodynamic parameters, the forces, including the normal force (F_n), tangential force (F_t), lift force (F_l), and drag force (F_d) [see Fig. 3(e)], can be calculated as

$$F_i = \int_P \rho\omega^2 C_i dSx^2 dx, \qquad i \in \{n, t, l, d\} \tag{1}$$

[2][Online]. Available: https://github.com/Ho-lab-jaist/tombo-propeller.git

where P is the designed span length function along the airfoils, ρ is the air density, ω is the rotational speed, $C_i = C_i(\theta)$ is the aerodynamics force coefficient function (see [41]), $\theta = \theta(x)$ is the designed pitch angle function [see Fig. 3(e)], S is the designed boundary surface function, and x is the span length element along the airfoils.

B. Role of Deformable Angles α, β, and γ

Although the flexibility of the *nodus* saves the propeller from collision damage, it creates unexpected deformation when the propeller rotates. In detail, when a rotor is rotating, rigid wing [see Fig. 3(d)] displacement is quantitatively specified by bending angles α and β and twist angle γ, as depicted in Fig. 3(d). These deformable angles alter the geometry of the propeller, such as pitch angle θ, inducing change in aerodynamic forces F_d and F_l. Therefore, an aerodynamic model Tombo propeller needs to factor in the deformable angles of the *nodus* in order to achieve the efficient operation of the device.

C. Nodus *Modeling*

To determine the deformable angles, we model both the material and the structure, i.e., morphology, of the *nodus* using the combination of composite and beam models.

1) Material Modeling: The structure of the *nodus* suggests a composite model of silicone rubber and a tendon playing the roles of material matrix and reinforced fibers, respectively [see Fig. 3(a)]. Based on research by Younes et al. [42] on different models for composite modeling, we chose the Chamis model for modeling because of its high accuracy for predicting elastic modulus coefficients in many matrix and fiber material cases. According to the Chamis model, the Young modulus E_N and the shear modulus G_N of *nodus* are defined as follows:

$$E_N = \frac{E^m}{1 - \sqrt{v^f}(1 - \frac{E^m}{Ef})}, \quad G_N = \frac{G^m}{1 - \sqrt{v^f}(1 - \frac{G^m}{G^f})} \tag{2}$$

where v^f is the fiber volume fraction, E^m and G^m are the Young modulus and the shear modulus of the matrix material, respectively, and E^f and G^f are the Young modulus and the shear modulus of the fiber material in turn, respectively. The fiber volume fraction v^f (from 0 to 1), measured as the percentage of fiber area in the composite cross section, dominates the mechanical properties of the *nodus*. Changing the number of fibers or their diameter adjusts fiber volume fraction v^f, resulting in a proportional change in *nodus* stiffness.

2) Structure Modeling: We hypothesized that the *nodus* deflects obeying cantilever beam behavior with one fixed end [see Fig. 3(b)] during its rotation. Therefore, the deformable angles can be defined in a model of a stationary cantilever (at a specific rotation speed) by applying the beam modeling. As a result, bending angles α in the Oxy plane and β in the Oxz plane of a Tombo propeller are defined based on [43] as follows:

$$\alpha = \frac{F^y_{BN} L^2_N}{2E_N I^z_N}, \qquad \beta = \frac{F^z_{BN} L^2_N}{2E_N I^y_N} \tag{3}$$

where F^y_{BN} and F^z_{BN} are forces from the wing applied to the *nodus*, L_N is the *nodus* length, E_N is the Young modulus of

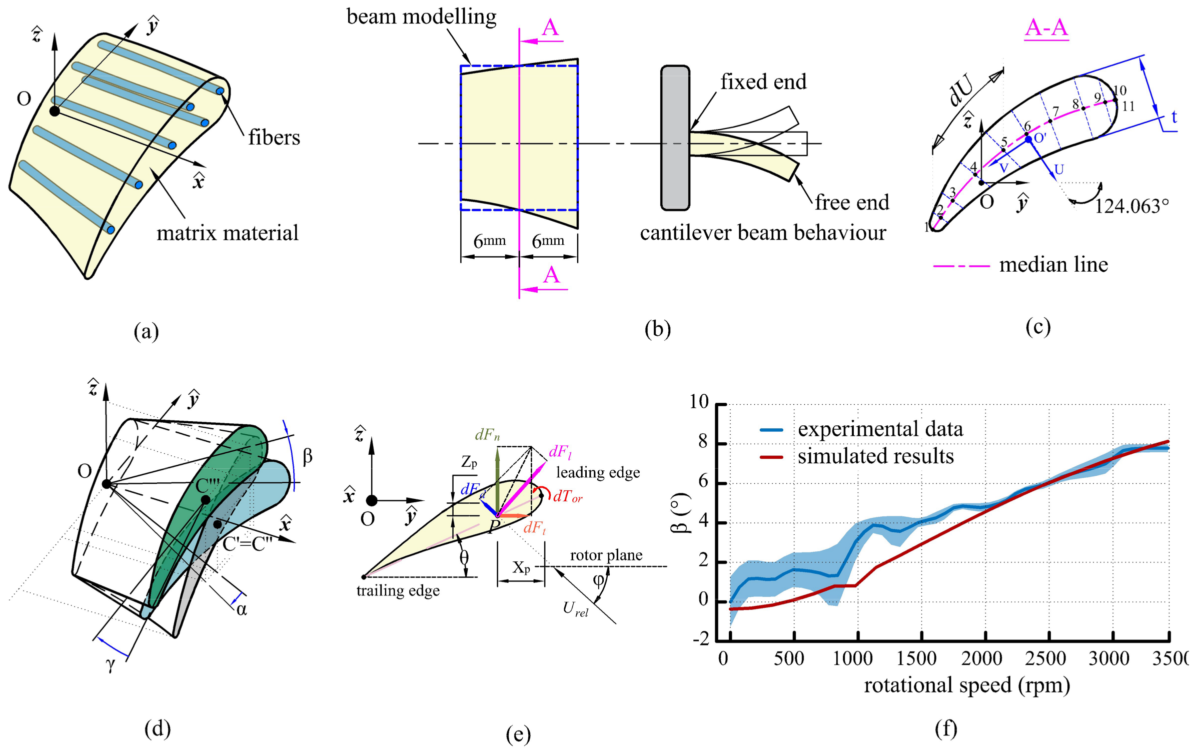

Fig. 3. *Nodus* modeling and evaluation of deformable angle β. (a) Body of the *nodus* can be described as a composite structure comprising reinforced fibers in a material matrix. (b) Cantilever beam with a cross section as the *representative cross section* stay at the center of the *nodus* length enables the deformable behavior of the nodus. (c) Parameters of the *representative cross section* include the key median line (or the mean camber line) interpolated by the ten point coordinates shown. (d) Deformable behavior of the *nodus:* 1) from C' to C'': rotated around OC'' by γ, and 2) from C'' to C''': rotated around Oz and Oy by α and β in turn. Note that O and C' are the center points at either end of the nodus. (e) *Enter of pressure* stays at the quarter chord of an airfoil. U_{rel} is the relative wind. (f) Simulated deformable angle β and the experimental data with reference to the rotational speed. (a) Composite structure of *nodus'* material. (b) Deformation of nodus as a cantilever beam deflection. (c) The *representative cross-section* parameters. (d) *Nodus* deformation represent in three deformable angles. (e) *Pressure center* of an airfoil. (f) Comparison of theoretical and practical deformable angle β.

the *nodus*, and I_N^y and I_N^z are the inertial moments of the cross section of the *nodus* in $\hat{y}$- and $\hat{z}$-directions, respectively. Since the inertial moments depend on the cross-section position, (3) shows a strong relationship between the *nodus* length and the cross-section position to deformable angles α and β.

3) Hybrid Modeling: To model the mechanical characteristics of the *nodus*, we used hybrid modeling combining insights of both aforementioned material and structural models. However, both the popular composite models reviewed in [42] and the beam model [43] often required the high homogeneity of materials and a standard cross-sectional area structure, while the *nodus* has different directions of nylon tendons and varying morphology along its body. Therefore, for ease of modeling, we proposed a *representative cross section* [see Fig. 3(c)], stay at the middle of the *nodus* [section A-A in Fig. 3(c)] to overcome this issue. This particular cross section will be used for all the related calculations of the *nodus*. The twist angle γ of a Tombo propeller can be defined as a form of elongated cross section as follows [44]:

$$\gamma = \frac{3\left(1+\dfrac{4F}{3A_N U^2}\right) T_{or} L_N}{G_N F} \tag{4}$$

where $F = \int_0^U t^3 dU$, dU is the infinitesimal length along the camber line, T_{or} is the applied torque generated by the aerodynamic forces F_d and F_t, A_N and U are the area and the length of a camber line of the *representative cross section*, respectively, L_N is the length of the *nodus*, and t is the thickness normal to the median line. If we call P is *the center of pressure* at *the quarter-chord point* of the airfoil [39], [45] [see Fig. 3(e)], then the applied torque element dT_{or} can be defined as follows:

$$dT_{or} = dF_t \frac{\mid y_{LE} - y_{TE} \mid}{4} + dF_d \frac{\mid z_{LE} - z_{TE} \mid}{4} \tag{5}$$

where y_{LE}, z_{LE}, y_{TE}, and z_{TE} are the coordinates of the leading edge and the trailing edge of the *representative cross section* in $\hat{x}$- and $\hat{z}$-directions, respectively.

D. Aerodynamic Model of the Tombo Propeller

At a rotational speed, we assumed that the deformable propeller morphology was unchanged. Therefore, the applied aerodynamic forces of a Tombo propeller can be calculated as in (1). Note that the optional deformable edge (4) of the Tombo propeller was assumed not to deform in our proposed aerodynamic model at rotational speed. Thus, the influence of the deformable edge is negligible in the computational model. Here, the functions of the span length, aerodynamic force coefficient, and the boundary surface were considered to be the main contributors to the deformable angles. In the model, the aerodynamic forces consist of three components generated by the hub and the *nodus*; therefore, these aerodynamic forces can be explained as follows:

$$F_i = F_i^h + F_i^N + F_i^w, \qquad i \in \{n, t, l, d\}. \tag{6}$$

The hub is rigid and the *nodus* length is about 10% of that of the propeller; therefore, we can use (1) to calculate both F_i^h and F_i^N. The aerodynamic force of the wing [39] for the Tombo propeller needs to take into account the contribution of the deformable angles as follows:

$$F_i^w = \int_{P^{de}} \rho\omega^2 C_i^{de} d(S^{de}) x^2 dx, \qquad i \in \{n, t, l, d\} \tag{7}$$

where P^{de} is the deformable span length function along the airfoils, $C_i^{de} = C_i(\theta^{de}(x))$ with θ^{de}(x) is the deformable pitch angle function of the Tombo propeller airfoil, S^{de} is the deformable boundary surface function, and P^{de} and S^{de} can be defined by the projections of the wing into the $\hat{x}$-direction and the Oxy plane, respectively, when the *nodus* deforms. Note that the wing posture can be defined by rotation matrix $\mathbf{R}(\alpha, \beta, \gamma) \in SO(3)$ using a roll–pitch–yaw sequence of rotations around axes of a fixed reference frame [46]

$$\mathbf{R}(\alpha, \beta, \gamma) = \mathbf{R}(\hat{z}, \alpha)\mathbf{R}(\hat{y}, \beta)\mathbf{R}(\hat{x}, \gamma) \tag{8}$$

where α and β are the bending angle functions of the *nodus* on Oxz and Oxy, respectively, γ is the twist angle around the centroid contour along the *nodus*, and $\mathbf{R}(\hat{x}, \gamma)$, $\mathbf{R}(\hat{y}, \beta)$, and $\mathbf{R}(\hat{z}, \alpha)$ are the rotations around the $\hat{x}$-, $\hat{y}$-, and $\hat{z}$-axes of the fixed reference frame [see Fig. 3(d)], respectively.

To simplify change in the boundary surface function, we project this wing into three original planes, i.e., Oxy, Oyz, and Ozx. Finally, we obtained the equation of aerodynamic forces applied to a wing as follows:

$$F_i^w = \int_{r_N}^{R} \rho\omega^2 C_i^{de} \frac{\cos\alpha \cos\beta \cos(\theta - \gamma)}{\cos\theta} (L - T)\, x^2 dx, \qquad i \in \{n, t, l, d\} \tag{9}$$

where r_N and R are the radius of innermost and outermost curvatures from the position of *nodus* onward, respectively, and L and T are the designed geometrical functions of the leading edge and the trailing edge, respectively.

To define functions L and T, we represent half of a propeller by 24 cross sections along the span [see Fig. 4] by SolidWorks 2020 software. In each section, we collected the angle of attack and the coordinates of leading edges and trailing edges by AutoCad 2022 software. Next, we applied the formula of L, T, and θ as the functions of span length using the *polyfit* function of MATLAB R2020b.

E. Numerical Implementation of the Aerodynamic Model

By its nature, the proposed model has an implicit problem because of the interdependencies between the input parameters. Nonlinear solution techniques can solve this problem, but using

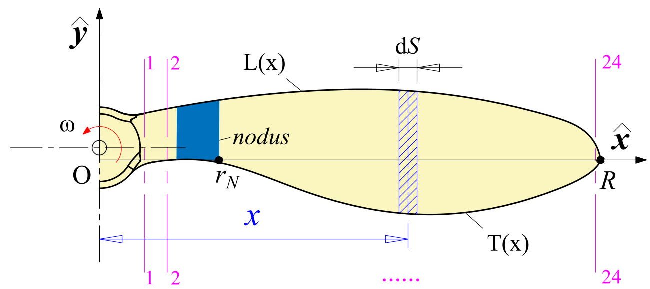

Fig. 4. Half of the designed propeller shows the boundary surface element $d(S)$ and the geometrical functions L and T. Magenta lines locate the positions of cross sections for collecting airfoil information.

Algorithm 1: Aerodynamics Parameter Estimation for Rigid Propellers.

Input: Airfoil parameters, air density ρ, and rotational speed of propeller n_r
$N :=$ number of cross sections
$S_C = \{S_i : [x_{C_i}, y_{LE_i}, z_{LE_i}, y_{TE_i}, z_{TE_i}, \theta_{C_i}]\} :=$ coordinate of leading edge and trailing edge, and pitch angle $i \in \{1, \ldots, N\}$
Output: Aerodynamics forces F_j, $j \in \{n, t, l, d\}$
//Separate geometric functions into parts by order
$k :=$ Number of geometrical function parts
$o_i :=$ Order of the ith part
$F_i := 0$
for $i := 1$ to k **do**
  $P_i :=$ polyfit$(x_C, y_{LE}, y_{TE}, o_i)$
  $F_j :=$ polyfit$(x_C, C_j(\theta_C), o_i)$
end for
return F_j

a simple algorithm where an iteration loop is used until convergence is reached is a more practical solution. Algorithms 1 and 2 have shown this approach in two cases: a classical propeller (the rigid one) and a Tombo propeller (see our Git project[3] for more details).

V. Measurement of Tombo Propeller's Characteristics

In this section, we describe indoor experiments with different configurations of *nodus* matrix materials and fiber diameters (see Table I) to determine the characteristics of Tombo propellers . These experiments were performed for the following purposes:

1) to evaluate the aerodynamic model proposed in Section IV based on the thrust force and deformation angle results;
2) to observe the characteristics of the Tombo propeller in action to acquire and build fundamental knowledge on this biomimetic propeller.

The experimental apparatus included an X2212 960-kV motor (to rotate the propeller) fed by a 12-V power source, which was mounted on a force gauge (IMADA ZTS-5N 10 Hz, Japan); an acrylic base plate to isolate the conductor and other parts (see

[3][Online]. Available: https://github.com/Ho-lab-jaist/tombo-propeller.git

Algorithm 2: Aerodynamics Parameter Estimation for Tombo Propellers.

Input: Airfoil functions, representative section, *nodus* parameters, air density ρ, and rotational speed of propeller n_r, loop options
$S_C, k, P_i, L, T :=$ Airfoil parameter and functions
$U_C, A_C, F :=$ *Representative cross-section* parameters
$E_N, G_N, I_C^x, I_C^z, x_N, L_N :=$ Young's and shear modulus, coordinate and length of *nodus*
$nbIt :=$ Maximum number of iterations
$Tol :=$ Acceptance tolerance
Output: Aerodynamics parameters F_j, C_j, $j \in \{n, t, l, d\}, Tor$, lift-over-drag ratio ε_{lod}
//LOOP
loop
  $\alpha = \alpha(F_d, E_N, I_C^z)$
  $\beta = \beta(F_t, E_N, I_C^x)$
  $T_{or} = T_{or}(F_{t2}, F_{d2}, \theta_C)$
  $\gamma = \boldsymbol{\gamma}(T_{or}, G_N, F_C)$
  $F_j^w = F_j(\rho, n_r, \theta_C, C_j, x_N, L_N), j \in \{n, t, l, d\}$
  //*Calculate the results*
  $F_j = F_j^h + F_j^N + F_j^w$
  //Convergence Criteria
  if $i > nbIt$ **then**
    break
  else
    if $|F_t - F_t last| + |F_d - F_{dlast}| < Tol$ **then**
      break
    end if
  end if
end loop
return F_j, C_j, T_{or}, and ε_{lod}

Section V-A; a high-speed camera (DSC-RX10M4, Sony, Japan) to record recovery time and deformable angle β measurements (see Sections V-C and V-D); and lighting and a black background to facilitate visual detection. The results of the experiments are presented and discussed in Section VI.

A. Thrust Force Measurement Experiments

In this experiment, we measured the thrust force of the Tombo propeller with reference to the rotational speed through the range 2000–3200 r/min with 13 configurations, as shown in Table I. The experiment was conducted indoors, and the axis of the motor was set vertical relative to the ground [see Fig. 5(a)]. The measurement sampling rate was 10 Hz.

B. Deformable Angle β Measurement Experiments

For this measurement, the high-speed camera (960 frames/s) was set perpendicular to the rotor plane and coincident with the rotor axis, as shown in Fig. 5(d).

Initially, we increased the speed of the rotor to a specific rotation speed; then, we started recording and reduced the rotor speed to 0 r/min. The recorded video was processed by OpenCV in Python and split into a series of still image frames, which appeared blurred [see Fig. 6(a)]. Next, we determined the rotational speed of the Tombo propeller in each image frame and the corresponding propeller diameter using a normalized ten-continuous-frame combo [see Fig. 6(b)]. To determine the propeller diameter at each combo, we needed to focus on the center of its rotation [see Fig. 6(c)]. Center detection initially attempted using the OpenCV function was poor because the generated coordinate must be an integer [see Fig. 6(d)]. We, then, transformed the coordinates of each pixel to the real field [see Fig. 6(e)]. From that, we utilized a RANdom SAmple Consensus (RANSAC) [47] algorithm to determine the appropriate center of a point cloud [see Fig. 6(f)]. We, then, could define the diameter of a ten-continuous-frame combo taking advantage of Hull's contour [see Fig. 6(g)]. Finally, the deformable angle β could be calculated based on change in diameter and the position of the *nodus* [see Fig. 6(h)]. Note that we omitted recorded image perspective distortions made by the change of propeller tip in the vertical direction due to the small increment of the camera angle of view δ_ψ (less than 1.2%).

C. Time Recovery Measurement Experiments

The objective of this experiment was to determine the recovery time of the Tombo propeller after a collision. In this experiment, we used a model artificial finger made of silicone rubber (Dragon Skin 30) with a nylon monofilament core [see Fig. 5(b)] and the high-speed camera to record the process of collision and the subsequent recovery of the propeller (for both rotational speed and thrust). This artificial finger was inserted manually from above the propeller and collided randomly with the Tombo propeller. The propeller recovery time in terms of thrust force was calculated from measurements by both the force sensor and the camera, while that in terms of rotational speed was determined from the video data. In addition, the experiment was conducted three times with each propeller, and the longest recovery time of a one-hit collision was reported. Sometimes, the propeller repeatedly hits the finger.

D. Collision Force Measurement Experiments

For consistent measurement, the direction of the collision force must coincide with the measurement axis of the force gauge. The ZTS-500N force gauge with a large force range (up to 500 N), and a tube (3 cm in diameter and 150 cm in length) was placed perpendicular to the motor plane [see Fig. 5(c)]. The principle of measuring the collision force was as follows. An obstacle was dropped freely inside the guide tube from the top end to collide with the propeller at a specific location, and the collision force was recorded by the force gauge.

This experiment was divided into two parts. In part 1, we determined the most dangerous crash zone on the propeller blade by colliding the object at different distances 50, 60, 70, 80, 90, and 100 mm from the center of the propeller (see Table II). The position at 90 mm from the center of the propeller was chosen to perform part 2 of the test due to its highest critical force per thickness (61.4 N/mm). In part 2, we measured the collision force over a range of Tombo propeller configurations from Conf. 5–13 (see Table I). The test results are summarized in Table III.

TABLE I
TOMBO PROPELLER CONFIGURATIONS USED TO EVALUATE THE AERODYNAMIC MODEL AND OBSERVE WORKING CHARACTERISTICS

Name	*Nodus*' configuration							Deformable edge materials	Size (inch)
	Matrix material	Fiber material	Number of fibers	Diameter of fiber (mm)	Length (mm)	Young's modulus E_N (MPa)	Shear modulus G_N (MPa)		
Conf. 0	-	-	-	-	-	-	-	-	9
Conf. 1	DragonSkin 10	Nylon 6	6	0.94	12	0.1542	0.0551	-	9
Conf. 2	DragonSkin 20	Nylon 6	6	0.94	12	0.5705	0.2036	-	9
Conf. 3	DragonSkin 30	Nylon 6	6	0.94	12	0.7873	0.2809	-	9
Conf. 4	DragonSkin 30	Nylon 6	6	0.38	12	0.6557	0.2341	-	9
Conf. 5	DragonSkin 10	Nylon 6	5	0.5	12	0.1315	0.0469	DragonSkin 10	9
Conf. 6	DragonSkin 10	Nylon 6	5	0.75	12	0.1413	0.0505	DragonSkin 10	9
Conf. 7	DragonSkin 10	Nylon 6	5	0.9	12	0.148	0.0528	DragonSkin 10	9
Conf. 8	DragonSkin 20	Nylon 6	5	0.5	12	0.4862	0.1736	DragonSkin 20	9
Conf. 9	DragonSkin 20	Nylon 6	5	0.75	12	0.5227	0.1866	DragonSkin 20	9
Conf. 10	DragonSkin 20	Nylon 6	5	0.9	12	0.5473	0.1954	DragonSkin 20	9
Conf. 11	DragonSkin 30	Nylon 6	5	0.5	12	0.671	0.2396	DragonSkin 30	9
Conf. 12	DragonSkin 30	Nylon 6	5	0.75	12	0.7213	0.2574	DragonSkin 30	9
Conf. 13	DragonSkin 30	Nylon 6	5	0.9	12	0.7552	0.2695	DragonSkin 30	9

1 - Tombo propeller
2 - IMADA force gauge ZTS-5N
3 - Brushless motor X2212 960KV
4 - Motor base
5 - Human finger model
6 - Sony high-speed camera DSC-RX10M4
7 - Optical breadboard
8 - Acrylic plate
9 - Guide tube
10 - Collided obstacle
11 - IMADA force gauge ZTS-500N
12 - Rope

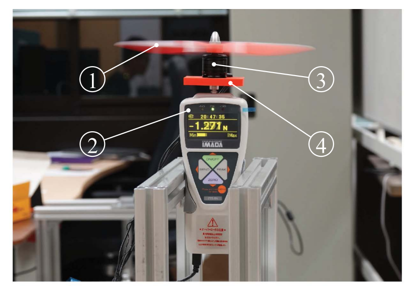

(a)

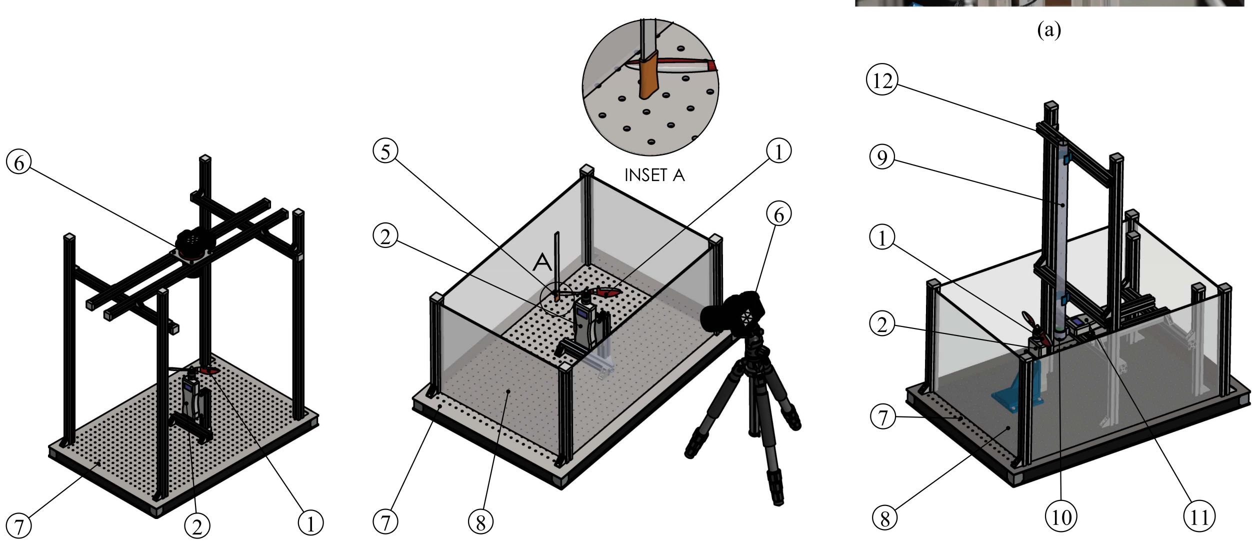

(b) (c) (d)

Fig. 5. Measurement setup for investigating the Tombo propeller characteristics. (a) Thrust force measurement experiments. (b) Deformable angle β measurement experiments. (c) Time recovery measurement experiments. Inset A shows the collision scenario between the propeller and the human finger phantom model. (d) Collision force measurement experiments.

TABLE II
COLLISION FORCE AND THICKNESS OF COLLIDED BLADE OF A TOMBO PROPELLER CONF. 13 AT 2500 R/MIN

Collision area	**I**	**II**	**III**	**IV**	**V**	**VI**
Distance to the hub center (mm)	50	60	70	80	90	100
Maximum collision force (N)	206.5	337.2	331.2	244.4	225.3	136.3
Thickness of the blade (mm)	6.2	6.2	6.0	5.3	3.7	2.8
Force per thickness (N/mm)	33.2	54.4	55.2	45.8	61.4	49.1

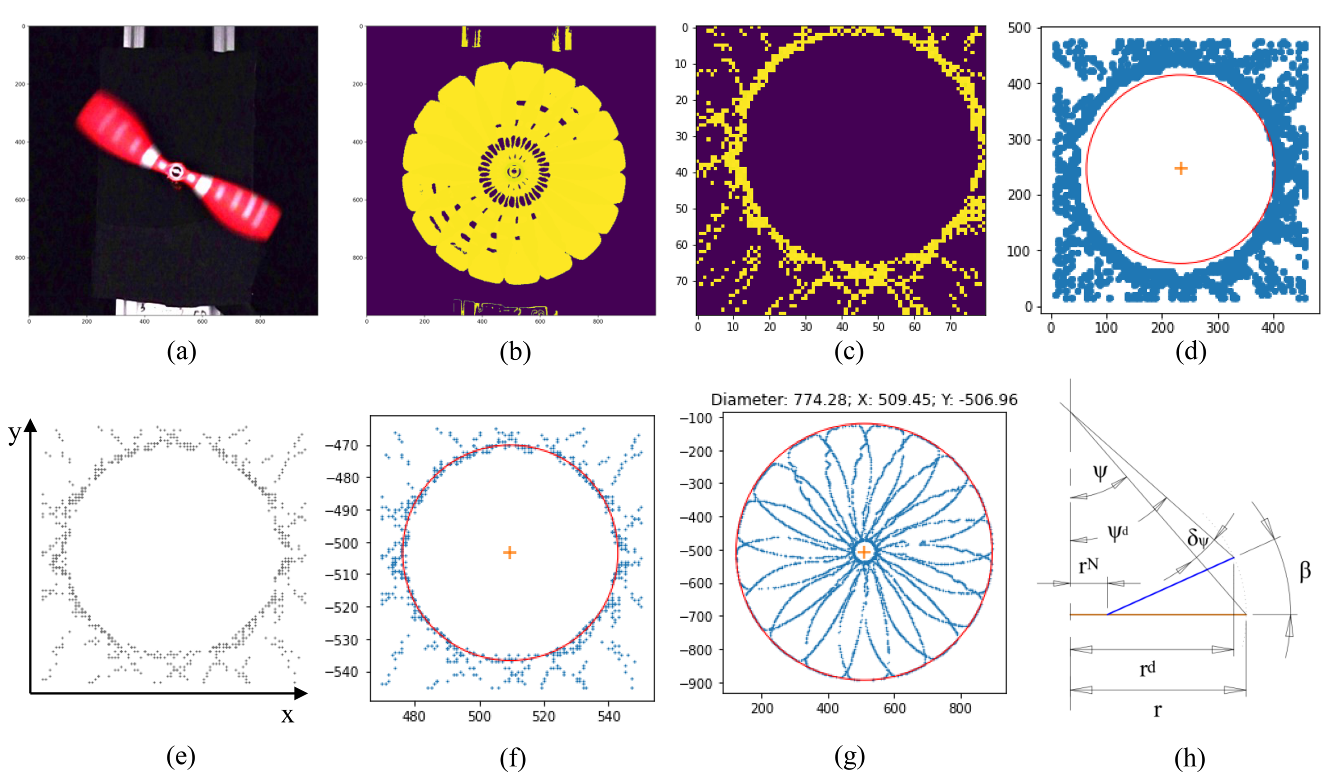

Fig. 6. Method of deformation angle β detection. (a) Images (blurred) were recorded of the high-speed-rotating propeller. (b) Ten-continuous-frame combo was used for speed normalization. (c) Center of a ten-frame combo image shows as a graph of pixels. (d) Failure of rotational center detection by the Open CV deployed function. (e) In transition from image processing to numerical processing, the pixel image is represented by a real number graph. (f) Result of rotational center detection by a developed function based on the RANSAC algorithm. (g) Owing to the convex Hull, the propeller diameter can be rapidly determined and visualized. (h) Definition of deformable angle as a function of propeller diameter change: $\beta = acos(\frac{r^d - r^N}{r - r^N})$, with r^d being the initial radius of a Tombo propeller, r is the radius of one in a deformed state, r^N is the distance from the center of the propeller to the start face of *nodus*, ψ and ψ^d are the camera view angles in rest and deformable states of the Tombo propeller, respectively, and $\delta_\psi = \psi^d - \psi$ is the change of camera view angles.

TABLE III
CHARACTERISTICS OF TOMBO PROPELLERS AND A RIGID PROPELLER MEASURED AT 2000 R/MIN OF ROTATIONAL SPEED

	Thrust force [N]	**Thrust force deviation [N]**	**Collision force [N]**	**Recovery time [s]**	**Simulated L/D ratio**	**Noise (distance: 5 m) [dB]**
Conf. 0	0.658	0.11	269.3	–	1.776	49.4
Conf. 5	0.656	0.03	147.3	0.63	2.0822	49.1
Conf. 6	0.537	0.14	93.7	0.55	2.0718	51
Conf. 7	0.631	0.04	81.5	0.32	2.0652	49.6
Conf. 8	0.589	0.09	80.4	0.32	1.9323	48.7
Conf. 9	0.622	0.07	159.6	0.3	1.9251	49.2
Conf. 10	0.656	0.12	123.7	0.66	1.9206	50.2
Conf. 11	0.666	0.07	123	0.39	1.9051	49.5
Conf. 12	0.624	0.26	189.9	0.55	1.899	52.4
Conf. 13	0.611	0.06	145.5	0.42	1.8952	50.7
Mean	0.621	0.098	127.2	0.46	1.9663	50.0

E. Noise Measurement Experiments

Noise is an important characteristic of a propeller, especially within a working scenario close to human. Therefore, we conducted this experiment to give more information and options to users for propeller choosing decisions. Here, the experiment employed a handheld Meter MK09 Sound Lever Meter measurement device. We recorded noises of single propellers from different distances: 1, 2, 3, 4, and 5 m. In this test, we used a rigid propeller and Tombo propellers with configurations, as shown in Table I.

VI. RESULTS

A. Aerodynamic Model of the Tombo Propeller

1) Nodus' *Parameters:* The mechanical and geometrical properties of the *nodus* are important parameters in the construction of an aerodynamic model propeller. Note that the *nodus* model presented in Section IV-C requires the following parameters: length of the *nodus*, representative cross-section information, number of fibers, diameter of fibers (from the design),

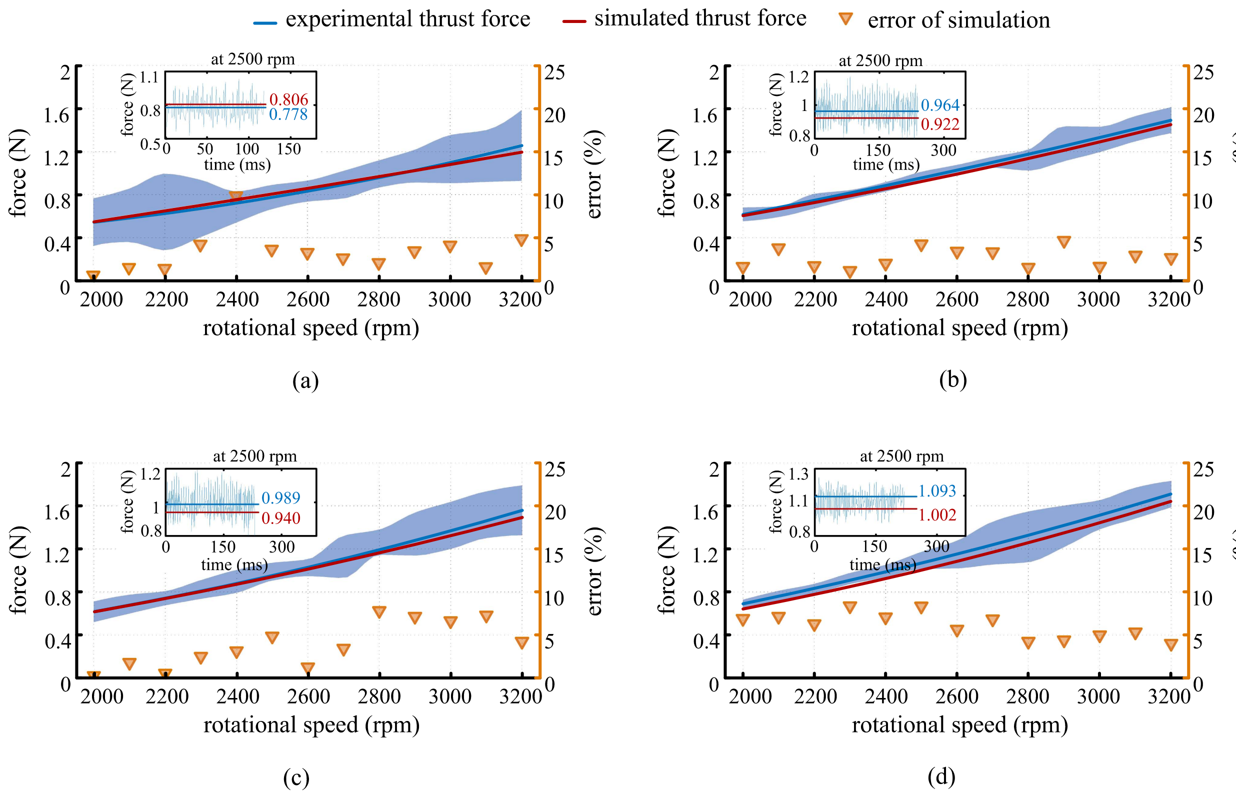

Fig. 7. Comparison of thrust and collision response among Tombo propellers with different *nodus* configurations. Experiments were conducted with three configurations of the Tombo propeller (Conf. 1, Conf. 2, and Conf. 3), and a rigid propeller (Conf. 0) in the speed range 2000–3200 r/min. The red line plots the estimated thrust force (EsT), the blue line depicts the experimental thrust force (ExT), and yellow triangles indicate the error of simulation. The subgraphs (in boxes within graphs a, b, c, and d) show the EsT and ExT of the propeller operating at a speed of 2500 r/min. (a) Comparison of theoretical and practical thrust force of Tombo propeller Conf. 1. (b) Comparison of theoretical and practical thrust force of Tombo propeller Conf. 2. (c) Comparison of theoretical and practical thrust force of Tombo propeller Conf. 3. (d) Comparison of theoretical and practical thrust force of Tombo propeller Conf. 0.

Young modulus, and shear modulus of the matrix material and fiber (from experiment results based on the American Society for Testing and Materials Standard—ASTM 412 Die D dumbbell specimens with the Poisson ratio was chosen as 0.4). Finally, the Young modulus and the shear modulus of the *nodus* were calculated using (2) and updated in Table I. The results indicated that the mechanical properties of the matrix play the most critical role in the calculation of Young modulus and shear modulus of the nodus. In addition, increasing the number and diameter of the fibers enhanced these moduli.

2) Tombo Aerodynamic Model: To evaluate the model, several experiments with different configurations of the Tombo propeller (see Table I) were conducted to compare estimated with experimental aerodynamic parameters. Fig. 7 shows evaluations of thrust force in the aerodynamic model for four different configurations of the Tombo propeller. First, the model showed good thrust prediction when estimation errors were less than 8% for different degrees of *nodus* stiffness. Second, as *nodus* stiffness increased, the magnitude and stability of lift force at the same speed increased. In the experimental rotational speed range (from 2000 to 3200 r/min), both the experimental and simulated thrust forces exhibited linear characteristics, but the simulation results in a broader range (up to 8000 r/min) showed more clearly the nonlinear characteristics [see Fig. 8(a)]. Moreover, Fig. 7 reveals that the propeller with less stiffness may induce larger vibration (thrust deviation) compared to the others (note that the noise of thrust forces can be from the vibration of the nodus, the deviation of the motor rotational speed, and the whole system). Therefore, we would recommend that the Tombo propeller should be checked after a long time of use to verify the stiffness changing of the *nodus* to decide whether the propellers should be replaced by the new ones.

This model can help to simulate the aerodynamic parameters of the Tombo propeller over a more extensive range of rotational speed. Fig. 8(a) shows the thrust force of rigid and Tombo propellers in the speed range below 18 000 r/min. Both the experimental and simulated results show that as the rotational speed gradually increases, the thrust force of the Tombo propeller remains proportional to *nodus*' stiffness, and at higher speeds, a significant difference is observed. Specifically, unlike the rigid propeller, the thrust force of each Tombo propeller configuration reaches the maximum at critical thrust T_{max} (in steady force state only) when the rotational speed is at ω_{mtf} (called *maximum thrust speed*). First, the rotational speed increases, leading to the rise of the deformable angle γ in the first phases I^1, I^2, and I^3 of Conf. 1, Conf. 2, and Conf 3, respectively [see Fig. 8(a)] for the notations of I^1, I^2, I^3, and so on). As a result, the lift coefficient (C_l) decreases. It is due to the fact that, in the first phase, since the ratio between the effect caused by rotational speed increase and that of C_l decrease was larger than one, the thrust force

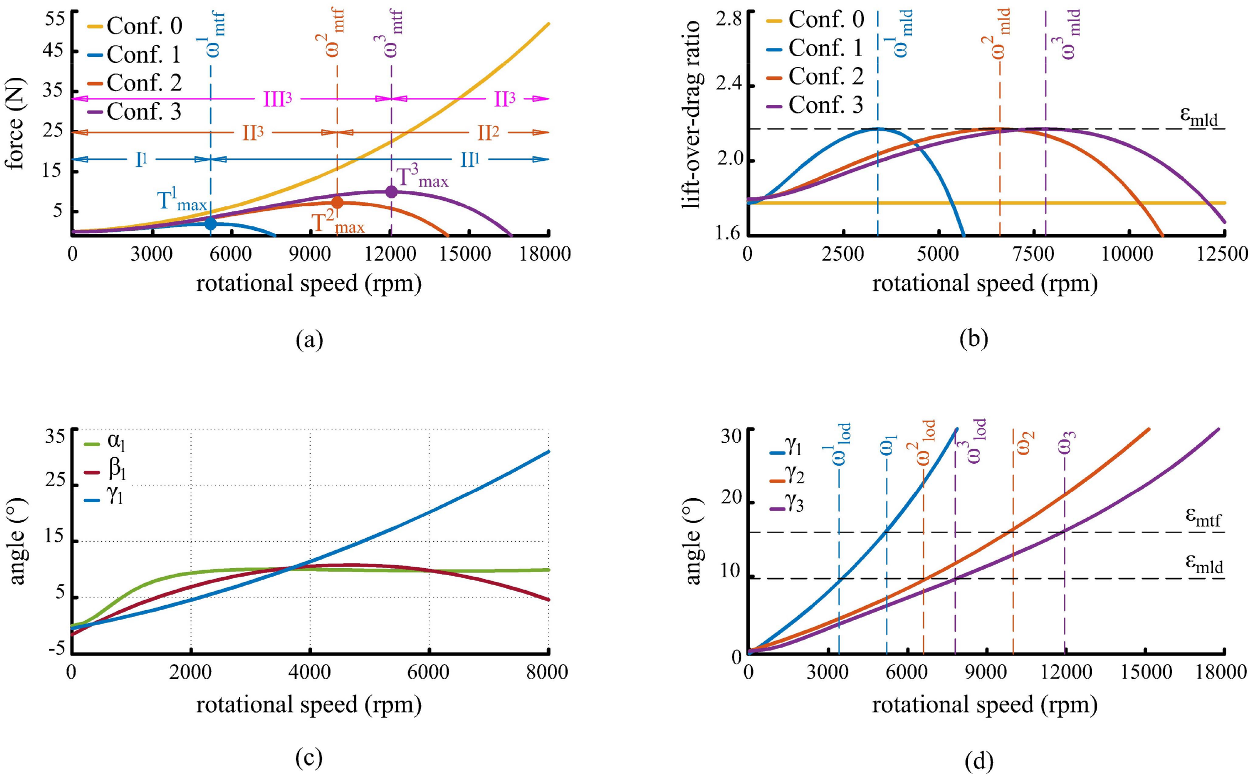

Fig. 8. Aerodynamic parameter estimations of the Tombo propeller by *nodus* stiffness. A rigid propeller (Conf. 0) and three Tombo propellers (Conf. 1, Conf. 2, and Conf. 3) were chosen for simulation. (a) We predicted thrust forces among the four configurations of the propeller in a larger range of rotational speed (up to 18 000 r/min) to discover the distribution of these forces. ω_1, ω_2, and ω_3 denote the rotational speeds of Conf. 1, Conf. 2, and Conf. 3, respectively, when the thrust force reached the maximum value. (b) Lift-over-drag ratio of Conf. 1, Conf. 2, and Conf. 3 Tombo propellers changed with rotor speed and reached the maximum value $\varepsilon = 2.17$ at rotational speeds $\omega^1_{\rm lod}$, $\omega^2_{\rm lod}$, and $\omega^3_{\rm lod}$, respectively. (c) Three deformable angles of Conf. 1 versus rotational speed of rotor. (d) Twist angle γ of Conf. 1, Conf. 2, and Conf. 3 shared the same value $\gamma_{\rm mtf}$ and $\gamma_{\rm mld}$ in both the cases of the maximum thrust force and the maximum lift-over-drag ratio. (a) Thrust force simulation of Tombo propellers Conf. 1, Conf. 2, and Conf. 3. (b) Lift-over-drag ratio simulation of Tombo propellers Conf. 1, Conf. 2, and Conf. 3. (c) Deformable angle simulation of Tombo propeller Conf. 1. (d) Distribution of deformable γ of Tombo propellers Conf. 1, Conf. 2, and Conf. 3.

keeps increasing. When the rotation speed is at $\omega_{\rm mtf}$, this ratio approaches one; thus, the thrust force reaches the peak $T_{\max}$. This critical thrust depends strongly on the *nodus* stiffness. The stiffer the *nodus* is, the higher the critical thrust force generated. In the second phases II^1, II^2, and II^3 of Conf. 1, Conf. 2, and Conf 3, respectively, when the rotational speed is higher than $\omega_{\rm mtf}$, since the aforementioned ratio is lower than 1, the thrust force decreases remarkably. Overall, this phenomenon suggests that $\omega_{\rm mtf}$ is a suitable choice for UAVs, which need to carry heavy loads or when high acceleration is required.

Fig. 8(b) shows the relationship between the lift-over-drag ratio $\varepsilon_{\rm lod}$ and the rotational speed of the Tombo propeller, simulated from (1) and (7) with $\varepsilon_{\rm lod} = F_l/F_d$. For rigid propellers, $\varepsilon_{\rm lod}$ independent of the rotational speed because the propeller geometry does not change during rotation. For the Tombo propeller, the coefficient $\varepsilon_{\rm lod}$ varied with rotational speed. However, as in the case of maximum thrust speed, each Tombo propeller has a *critical lift-over-drag ratio rotational speed* $\omega_{\rm mld}$, where $\varepsilon_{\rm lod}$ reaches the maximum (denoted $\varepsilon_{\rm mld}$). In other words, $\varepsilon_{\rm mld}$ is independent of the configuration of the Tombo propeller being the same for all the fabrication configurations. The reason is that these configurations all have the same initial geometric design, so when deformed, these configurations, even though they differ, will interfere in the state with the highest $\varepsilon_{\rm lod}$ result. This critical lift-over-drag velocity $\omega_{\rm mld}$ is variable between Tombo propellers and tends to increase with *nodus* stiffness. Therefore, $\omega_{\rm mld}$ can be chosen for the high efficient work of UAVs, such as traveling or delivery tasks.

From (3) and (4), we can predict the deformable angles of the Tombo propeller. For instance, Fig. 8(c) shows the simulation of these angles in a Conf. 1 propeller. It can be seen that as the propeller rotational speed increased, angles α and β increased rapidly to reach a stable value of about 10° in the speed range from 2000 to 5000 r/min. Meanwhile, γ continued to increase rapidly showing no sign of saturation. Combined with (9) and Fig. 8(a), this result demonstrated the significant contribution of γ to the thrust force of the Tombo propeller. To confirm the simulated variation of these deformable angles, we experimented with angle β using a Conf. 4 Tombo propeller [see Fig. 3(f)]. This experiment showed simulated angle β was similar to the experimental angle at a rotational speed range above 2000 r/min. In the lower speed range, the observed angle changed more strongly due to a limitation of the experimental model [see Section V-B]. When the speed of the motor rotating the propeller was decelerated suddenly, the inertia force caused

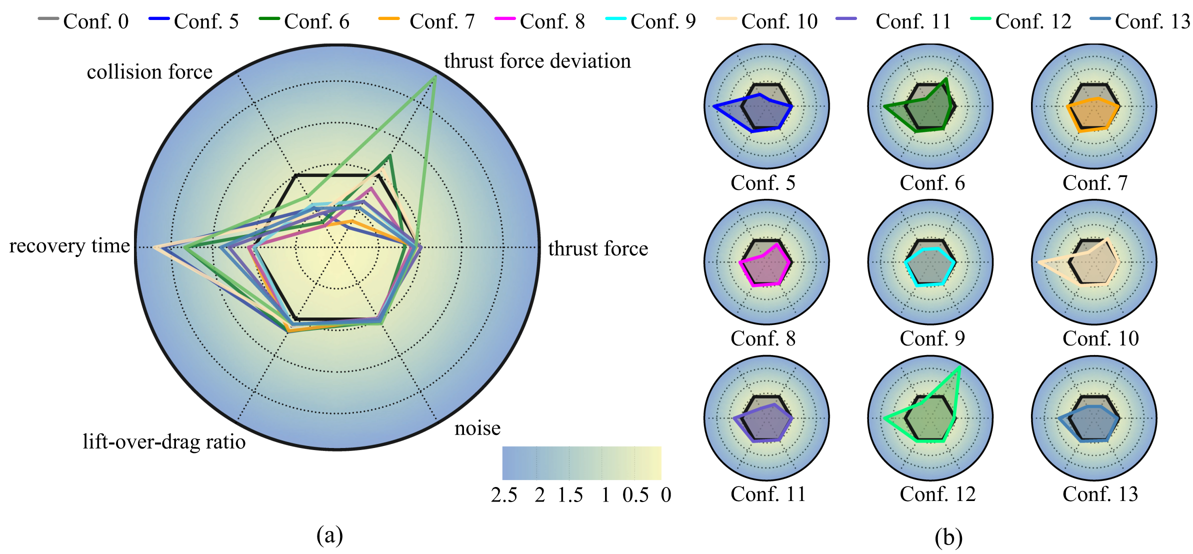

Fig. 9. Comparison of characteristics among nine configurations of a Tombo propeller and a rigid propeller (normalized by metrics of the rigid propeller). (a) Overview of nine configurations (see Table I) of the Tombo propeller (colored lines) and a rigid propeller (black line) of the same morphology. (b) Metrics of each configuration Tombo propeller in comparison with the rigid propeller. Details of metrics can be found in Table III. (a) Characteristics of nine Tombo propellers from Conf. 5 to Conf. 13 in comparison with that of the rigid one Conf. 0. (b) Characteristics of each Tombo propeller.

blade flapping at a rotational speed approaching zero, leading to a significant change in the deformable angle.

To investigate the contribution of γ to the aerodynamic of the Tombo propeller, we simulated this angle, as shown in Fig. 3(f). Despite different configurations, the Tombo propeller, which shares the same original design, will reach critical thrust and critical lift-over-drag ratio states at the same γ_{mld} and γ_{mtf}. This finding strongly confirms that γ plays the decisive role in the deformable states of the Tombo propeller.

B. Characteristics of the Tombo Propeller With Different Configurations

As mentioned above, the Tombo propeller is a deformable propeller for UAVs, which was designed to contribute to ultimate safety. Therefore, it was important to investigate its characteristics to clarify and confirm its contributing features. Nine configurations of the Tombo propeller and a rigid one were analyzed focusing on six characteristics: thrust force, thrust force deviation, collision force, recovery time, simulated lift-over-drag (L/D) ratio, and noise (see Table III). All the experiments were conducted at a propeller rotation speed of 2000 r/min, and data were normalized by the results of the rigid propeller (Conf. 0) for visualization, as in Fig. 9.

Overall, the Tombo deformable propeller shows promising characteristics compared to a rigid one. While all of thrust force, thrust force deviation, simulated L/D ratio, and noise of the experimental Tombo propellers (0.621 N, 0.098 N, 1.9663, and 50 dB, respectively) are almost the same as those of the rigid propeller (0.658 N, 0.11 N, 1.776, and 49.4 dB, respectively), thrust force deviation, collision force, and time recovery all differed. Note that although the mean of the thrust force deviation of the Tombo propeller was lower than that of the rigid propeller, its distribution was extensive, ranging from 0.03 to 0.26 N among different configurations. Practical flights showed that thrust force deviation played a vital role in creating the balance of a drone; therefore, the configuration needs to be considered to equip a drone. Last but not least, the collision force of the Tombo propeller was much smaller than that of the rigid propeller, resulting in the lower risk of injury or damage upon collision with an obstacle in its surroundings.

VII. Tombo Propeller in Practical Flights and Its Responsiveness to Midair Collisions

This section examines how the Tombo propellers behave in practical flight when equipped in drones [quadrotors, see Fig. 10(a)], as well as how the controller responds during and after a collision between the Tombo drone and a fixed midair obstacle. We chose Tombo propellers Conf. 13 to conduct the experiments in this section because they have a low thrust deviation (see Section VI-B) and one of the highest stiffness of the *nodus* and the deformable edge (see Table I), resulting in ease of fabrication and high consistency among fabricated propellers. In our observation, higher stiffness gives better flying performance but results in higher collision force, which should be strongly considered in the design. Note that we chose this suitable configuration among the successful fabrication ones to conduct this experiment as a showcase, but it is not considered as optimal one. Ones are expected to sort out the most suitable one for their application based on our analysis. In addition, to leverage the self-recovery ability of our deformable propellers, we implemented an equilibrium bounce reaction scheme [37], which was specifically tailored to rescue the Tombo drone (quadrotor) from a sudden fall in event of propeller–obstacle collision.

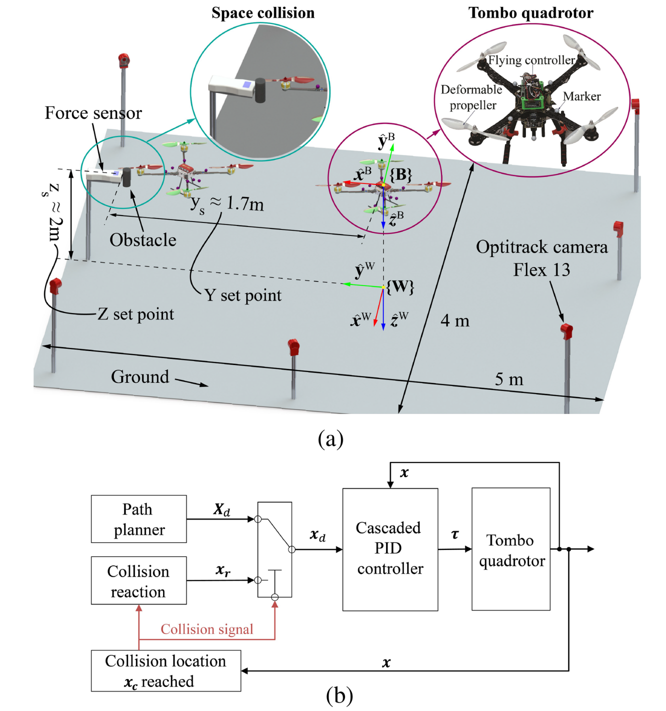

Fig. 10. Experimental setup for drone flight experiments. (a) Indoor environment and setup for flight tests and collision experiments, in which the OptiTrack Mocap system (for motion picture and 3-D tracking) was used to determine the position of the Tombo quadrotor. (b) Schematic of the reaction strategy, which was implemented in response to a collision between the Tombo propeller and a fixed obstacle. (a) Indoor environmental setup for flying experiments. (b) Implementation of bounce reaction strategy.

A. Reaction Strategy

In pursuit of drone safety provided by deformable propeller recovery, we investigated an equilibrium bounce reaction strategy expected to prevent the Tombo quadrotor from falling in event of a propeller–obstacle collision. We considered a case where the quadrotor flew at designated trajectory $\mathbf{X}_d$ such that one of the front propellers collided with a midair obstacle located at designated position $\mathbf{x}_c \in \mathbb{R}^3$ with reference to the global $\{W\}$ coordinate frame [see Fig. 10(a)]. Once $\mathbf{x}_c$ reached, collision occurred; the reaction mode was immediately triggered to set the equilibrium position to $\mathbf{x}_r = \mathbf{x}_c + d_r \mathbf{n}_r$, where $d_r > 0$ is the bounce distance and $\mathbf{n}_r$ is the reactive normal that is opposite to the flying direction before the time of collision. This encourages the low-level controller to produce virtual forces that drive the quadrotor toward equilibrium state $\mathbf{x}_r$ and then enable the stabilization of the vehicle at a safe distance from the obstacle. Since the falling rate of the quadrotor, as observed in experiments, was determined to be around 0.3 m/s, and the propeller recovery time was determined to be approximately 0.42 s, a typical proportional–integral–derivative (PID) cascaded controller could be a possible solution for low-level control. The cascaded control architecture of the quadrotor includes an outer loop P position, followed by the P angle, and PID angular rate controllers, running at 50 Hz, 250 Hz, and 1 kHz, respectively. The equilibrium bounce reaction strategy is summarized in Fig. 10(b), and we open source the implementation of the reactive control strategy using the robot operating system [48], as follows in our Git project.[4]

B. Experimental Setup

Fig. 10(a) illustrates the indoor environment, where the flight and collision experiments were conducted. Inside the experimental space, the custom-built quadrotor, equipped with four Tombo propellers and mounted with eight reflective markers, was precisely positioned by the *OptiTrack* motion capture system (mocap) including six tracking cameras (OptiTrack Flex 13), which provide an overall positional accuracy up to 1.2 mm. The quadrotor's six-DoF pose (i.e., position and orientation), estimated by the mocap system on a desktop PC (Intel i7-7700 CPU at 3.6 GHz and 8-GB RAM), was communicated to an onboard computer (Jetson TX2, NVIDIA) at around 30 Hz so that the automatic flight and collision reaction scheme can be practically implemented in real time, with the assistance of the PID-based low-level controller (PX4 flight stack[5]) running on the *Pixhawk 4* autopilot hardware. While the real-time postural information provided feedback signals for the P position and angle controllers, the onboard inertial measurement unit was responsible for the most inner PID control loop of the angular rate.

C. Results: Flying Behavior, Collision Response, and Recovery

To investigate the responsiveness of the Tombo propeller and effectiveness of the bounce reaction (recovery process) scheme upon the aforementioned collision, we set up a flight test wherein the quadrotor flew along planned trajectory $\mathbf{X}_d$ in the $\hat{y}$-direction such that the front port (left) propeller collided with an obstacle located at position $\mathbf{x}_c = [0.0,\ 1.7,\ -2.0]^{\mathrm{T}}$ m. Upon the collision, we set the bounce distance $d_r = 0.8$ m, leading to the equilibrium position at $\mathbf{x}_r = [0.2,\ 0.9,\ -2.0]^{\mathrm{T}}$ m, for the activation of the recovery process. The Tombo quadrotor, as observed from the experiments (see Fig. 11), could achieve stable flights as it can track the specified reference trajectory of position $\mathbf{X}_d$ during the hovering and precollision (flying along the y-direction) phases [see Fig. 11(c)]. The quadrotor started to fall when a propeller collided with the obstacle. Without the application of the reaction scheme, the drone could not recover and would fall and crash [as shown in Fig. 11(a)]. In contrast, the application of the bounce reaction strategy, in addition to the fast recovery of the Tombo propeller, allowed the quadrotor to stabilize in response to the collision [see Fig. 11(b)]. Fig. 11(c) details the behavior of the quadrotor during the collision and recovery process. Specifically, once the collision occurred at around $t_c = 23$ s, the quadrotor oscillated and overturned with a large fluctuation in roll angle and then started to fall, which characterizes the unstable phase. However, the quadrotor did not fall to the ground (collision height 2 m). It took about 1.5 s to overcome the unstable phase, followed by a recovery process of about 3.5 s before attaining a stable state, which confirmed the

[4][Online]. Available: https://github.com/Ho-lab-jaist/tombo-propeller.git
[5][Online]. Available: https://px4.io/

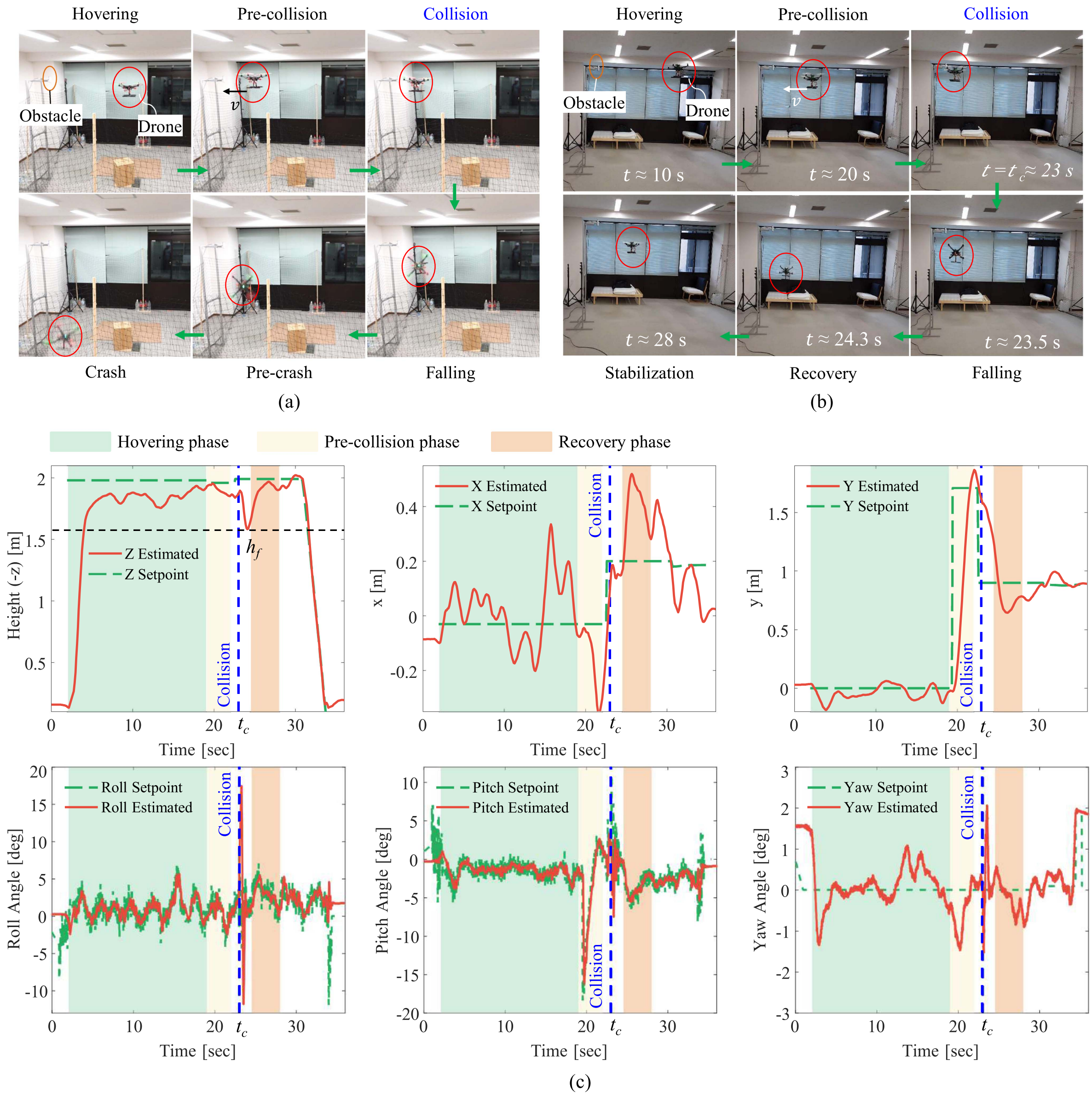

Fig. 11. Examination of the equilibrium bounce reaction of a quadrotor upon a Tombo propeller–obstacle collision. (a) Without implementation of the reaction strategy, the quadrotor completely crashed to the ground after a collision. (b) Video stills demonstrate the effectiveness of the reaction strategy, which could stabilize the quadrotor within 5 s. (c) Logs of the quadrotor state in terms of position and orientation during the flight and collision experiments show at collision time t_c, the reaction control mode was triggered and attempted to stabilize the quadrotor at a safe position $\mathbf{x}_r = [0.2,\ 0.9,\ -2.0]^{\mathrm{T}}$ m. (Note that the height of the quadrotor is minus z-coordinate). (a) Quadrotor's behaviour *without* reaction strategy. (b) Quadrotor's behaviour *with* reaction strategy. (c) Quadrotor's states during collision experiment.

responsiveness of the Tombo propeller and the effectiveness of the reaction strategy in event of collision with an obstacle. Since the drone trajectory was planned in point-to-point manner, during the recovery, the drone position would follow a straight-line path toward the predefined equilibrium position, starting from the lowest falling point at which the orientation had been restored to its initial state. The demonstration of the collision experiment can be found in the video.[6]

Consequently, in this section, we confirmed the flight ability of the drone with the Tombo propeller in a real platform and the recovery ability after the collision. In addition, the obtained results reveal that with the minimal invasion of the classical control strategy, the drone with the Tombo propeller still can perform basic flight/hovering and novel reaction upon collision with the surrounding. As a result, the introduction of softness to the propeller not only decreases the risk of damage, but also does not necessarily compromise the flight ability of the drone.

[6][Online]. Available: https://youtu.be/zjHvukgfJwc

VIII. Discussion

A. Efficiency

Regarding the efficiency loss, we have made a comparison between the Tombo propeller and other commercial 9-in propellers from UIUC Propeller Data Site[7] by the calculation of their L/D ratio at various rotation speed. Although the Tombo propeller has a slightly smaller efficiency compared to others (for example, Tombo propeller L/D ratio $= 2.16$ at 3000 r/min in comparison with 2.5 and 2.52 of the APC slow-flyer and GWS slow-flyer, respectively), we believe that the efficiency of the Tombo propeller still has room for improvement in terms of design and fabrication, as shown in the next section. At the research stage, we aimed for a thick airfoil propeller (i.e., slow-flyer propellers), since it is considered suitable for relatively large flying robots whose rotors perform at a low rotational speed. In addition, the Tombo propeller with the flexible nodus requires a thick airfoil to ensure a relatively stiff structure for stable working (with small deformation and vibration).

B. Design and Fabrication

The integration of soft materials into a conventional propeller improved safety in the operation of drones, especially by recovery ability and risk mitigation upon collision. The process of embedding tendons into the matrix by gluing them into the rigid parts (hub and wing) required significant manual dexterity. This, in fact, affects the quality of the fabricated propeller, thus decreasing its durability in long-term usage. Toward the mass production of the Tombo propeller, the proposed fabrication process in this research needs to be automatically conducted in as a manufacturing process. The most difficult task is the placement of tendons (fibers) during the assembly of the Tombo propeller. This process, in fact, can be automated with hole processing heat-welding-based assembly of tendons into holes of rigid parts (hub and blade). In addition, the rigid parts can be all made from injection molding toward high rigidity, smoothness, and consistency (rather 3-D-printed parts). With this process, the mass production of the Tombo propeller can be implemented, resulting in increased efficiency and durability. Moreover, we found that during rotation, the entire Tombo propeller from the hub to the tip became quite stiff due to centrifugal force through evaluation experiments. Therefore, if the connection between the *nodus* and the rigid parts is assured, the tendons used in the present design could be made redundant. For example, the double injection method may be exploited for the mass production of the Tombo propeller, since this technique can create a dependable junction between the soft *nodus* and the rigid parts, as well as the longevity of the propeller. In addition, this method is expected to result in high-quality Tombo propellers with low manufacturing costs, which benefits both the manufacturer and the user. More elaboration on this approach will be conducted in the future work.

In our current design, thick airfoils were chosen for ease of manufacturing, especially the fabrication and assembly of the *nodus* part. However, users with interest in the Tombo propeller may consider choosing suitable airfoils to develop their own deformable propellers. While the current design may result in higher cost and manufacturing difficulty, which can be tackled as mentioned in the above discussion, the efficiency of the Tombo propeller can be improved by applying high-performance airfoil for the blade parts. Regardless of that, experimental results presented in this article prove that the Tombo propeller can accommodate multidirectional collisions (see the attached video) and reduce remarkably the impact force on surrounding objects (see Fig. 9) thanks to its unique design. These advantages result in better collision adaptation compared to the traditional rigid propellers. In fact, the Tombo propeller is also durable enough for actual flight scenarios. Moreover, we have conducted an experiment on durability to show that a Tombo still operates after ten collision events. Note that the propeller repeatedly hits the obstacle even within an event. Regarding the scalability, we have succeeded in the fabrication of a wide range of Tombo propellers, such as 5-, 9-, 10-, and 20-in-long propellers, based on the proposed design and fabrication method. The durability experiment, the scalable fabricating results, and the flying performance of 5-in Tombo propeller equipped drone can be found in our video.[6] Smaller or bigger size and shape of the propeller will be investigated in the future. As a result, the proposed design of the Tombo propeller can be scaled, which brings in many options to users. Consequently, even the Tombo propellers may have several cons in terms of efficiency, its inherent flexibility and resiliency bring in more potential pros toward ultimate safety for drones.

C. Flight Ability

The results obtained in experiments revealed, for the first time, the successful flight performance and collision recovery behavior of a drone with a deformable propeller. However, there were some limitations in this study. The experiment trials were performed indoors, which ignores outdoor factors, such as wind and weather conditions. In addition, although PID controllers might achieve better performance in rigid propellers, due to the shortcomings of typical PID controllers, tracking errors in normal flight with deformable Tombo propellers were relatively large in some cases, especially in the $\hat{x}$-direction [see Fig. 11(c)], which led to different collision directions among flight trials and to various recovery behaviors (shown in the video at the link above). In addition, the fabricated propellers might not have yielded consistent behavior, which may have affected the controller's operation. In fact, the results shown in this article present the most typical drone behavior in response to the critical case of collision and to provide a benchmark against reactive performance. The average falling recovery time $\Delta t_{\text{recovery}} = 5$ s and the averaged maximum falling distance $\Delta h_{\text{fall}} = 0.5$ m were acceptable for this control strategy, considering that the midair collision height was 2 m indoors. For higher altitudes, there would be more time, thus a better chance for the drone to fully recover before crashing to the ground. That leaves room for work in the future improvement of the reaction control algorithms (e.g., model-predictive control and impedance/admittance reactive controllers [37]) since the recovery time of the tested propellers (≈ 0.46 s) was shorter than the current time for falling recovery (≈ 5 s). To this end, in future work, we aim to construct a comprehensive dynamics model of quadrotors that takes the aerodynamic modeling of Tombo propellers into consideration,

[7][Online]. Available: https://m-selig.ae.illinois.edu/props/propDB.html

which forms the foundation for advanced model-based interaction and tracking controllers and also for morphological design optimization. Moreover, the integration of perception to detect and avoid potential collisions is crucial to the realization of fully autonomous agile and resilient flying robots, which will be considered in future work.

D. Possible Applications

The Tombo propellers are expected to be equipped on drones for reducing the damage risk of obstacle–propeller collision in any direction. It also brings in the recovery chance after collision, thus mitigating risk to the drone itself and properties on the ground compared to crashing to the ground. The use of the Tombo propellers with other measurements will ultimately increase the safety of drones in tasks close to objects or humans (infra inspection, freight, and so on). For example, the drone with Tombo propellers can operate in the cluttered environment, such as forest or mountainous area, thanks to its recovery ability from unavoidable collisions. In the near future, it is expected that this application of the Tombo propeller will become more obvious when UAV delivery services take place in a more complex environments (buildings, residential areas, and so on) that require a high level of safety. In addition, drones with Tombo propellers can be widely used in the entertainment field, such as in drone shows, where drones fly close one to another that may increase the likelihood of mutual collision, or in the drone–human interaction scenario [49], [50]. Moreover, we would also like to adopt this biomimetic approach for applications in other sectors, such as small-scaled wind power generation propellers (reducing bird-strike risk), agricultural machine cutting blade (limiting damage of collision with rocks or broken branches), or ship propellers (reducing entanglement with marine litter, fish-strike risk, or even dangerous accidents to divers) toward sustainable solution for the nature.

IX. Conclusion

In this article, we proposed the design and fabrication of a biomimetic propeller. This approach can be applied to different types of propellers (e.g., flapping wing and glider wings). The proposed aerodynamic model showed to correctly estimate the propeller parameters, including thrust force and deformation angle in the plane perpendicular to the rotor plane. An examination of the characteristics of the Tombo propeller clarified the features and practicality of using this novel design for different vehicles. In addition, multiple flight experiments also demonstrated the ability of the Tombo propeller to increase drones' resilience to collisions, while concurrently preserving its mechanical structure after the impact. In the future, we aim to enhance the aerodynamic model of the Tombo propeller taking into account the contribution of the deformable edge. Furthermore, we would like to develop a software application leveraging this aerodynamic model to automatically produce aerodynamic metrics and automatically recommend a biomimetic design for a conventional propeller as an output to the user.

IX. Acknowledgment

The authors would like to thank Dr. Pho Van Nguyen for his advice on the modeling approach and Dr. David Price for his thorough proofreading of this manuscript. The authors also deeply thank anonymous reviewers of this article for valuable comments.

References

[1] *Unmanned Aerial Vehicle (UAV) Market by Product Type, by Wing Type, by Operation Mode, by Range, by Maximum Takeoff Weight, by System, by Application, by End-User, Forecasts to 2027*, Emergen Research, Vancouver, BC, Canada, 2020.

[2] M. Ayamga, S. Akaba, and A. A. Nyaaba, "Multifaceted applicability of drones: A review," *Technol. Forecast. Social Change*, vol. 167, 2021, Art. no. 120677.

[3] H. Rajabi, N. Ghoroubi, K. Stamm, E. Appel, and S. Gorb, "Dragonfly wing nodus: A one-way hinge contributing to the asymmetric wing deformation," *Acta Biomaterialia*, vol. 60, pp. 330–338, 2017.

[4] A. M. Mountcastle and S. A. Combes, "Biomechanical strategies for mitigating collision damage in insect wings: Structural design versus embedded elastic materials," *J. Exp. Biol.*, vol. 217, no. 7, pp. 1108–1115, 2014.

[5] R. J. Wootton, "Functional morphology of insect wings," *Annu. Rev. Entomol.*, vol. 37, no. 1, pp. 113–140, 1992.

[6] H. Rajabi, J.-H. Dirks, and S. N. Gorb, "Insect wing damage: Causes, consequences and compensatory mechanisms," *J. Exp. Biol.*, vol. 223, no. 9, 2020, Art. no. jeb215194.

[7] D. Q. Nguyen, G. Loianno, and V. A. Ho, "Towards design of a deformable propeller for drone safety," in *Proc. 3rd IEEE Int. Conf. Soft Robot.*, 2020, pp. 464–469.

[8] G. Chen, W. Dong, X. Sheng, X. Zhu, and H. Ding, "An active sense and avoid system for flying robots in dynamic environments," *IEEE/ASME Trans. Mechatronics*, vol. 26, no. 2, pp. 668–678, Apr. 2021.

[9] K. N. McGuire, C. D. Wagter, K. Tuyls, H. J. Kappen, and G. C. H. E. de Croon, "Minimal navigation solution for a swarm of tiny flying robots to explore an unknown environment," *Sci. Robot.*, vol. 4, no. 35, 2019, Art. no. eaaw9710.

[10] B. Herissé, T. Hamel, R. Mahony, and F.-X. Russotto, "Landing a VTOL unmanned aerial vehicle on a moving platform using optical flow," *IEEE Trans. Robot.*, vol. 28, no. 1, pp. 77–89, Feb. 2012.

[11] M. Iacono and A. Sgorbissa, "Path following and obstacle avoidance for an autonomous UAV using a depth camera," *Robot. Auton. Syst.*, vol. 106, pp. 38–46, 2018.

[12] N. Gageik, P. Benz, and S. Montenegro, "Obstacle detection and collision avoidance for a UAV with complementary low-cost sensors," *IEEE Access*, vol. 3, pp. 599–609, 2015.

[13] L. González-deSantos, J. Martínez-Sánchez, H. González-Jorge, F. Navarro-Medina, and P. Arias, "UAV payload with collision mitigation for contact inspection," *Autom. Construction*, vol. 115, 2020, Art. no. 103200.

[14] H. Li, W. Kinsner, Y. Wang, B. Palma, and A. Tay, "Airborne radar based collision detection and avoidance system for unmanned aircraft systems in a varying environment," in *Proc. IEEE Int. Conf. Wireless Space Extreme Environ.*, 2021, pp. 43–48.

[15] M. C. P. Santos, C. D. Rosales, M. Sarcinelli-Filho, and R. Carelli, "A novel null-space-based UAV trajectory tracking controller with collision avoidance," *IEEE/ASME Trans. Mechatronics*, vol. 22, no. 6, pp. 2543–2553, Dec. 2017.

[16] A. S. Huang, A. Bachrach, M. Krainin, D. Maturana, and N. Roy, *Robotics Reseach* (ser. Springer Tracts in Advanced Robotics), vol. 100, Cham, Switzerland: Springer, 2017.

[17] S. U. Sharma and D. J. Shah, "A practical animal detection and collision avoidance system using computer vision technique," *IEEE Access*, vol. 5, pp. 347–358, 2017.

[18] D. Falanga, K. Kleber, and D. Scaramuzza, "Dynamic obstacle avoidance for quadrotors with event cameras," *Sci. Robot.*, vol. 5, no. 40, 2020, Art. no. eaaz9712.

[19] A. Klaptocz, A. Briod, L. Daler, J.-C. Zufferey, and D. Floreano, "Euler spring collision protection for flying robots," in *Proc. IEEE/RSJ Int. Conf. Intell. Robots Syst.*, 2013, pp. 1886–1892.

[20] P. Kornatowski, S. Mintchev, and D. Floreano, "An origami-inspired cargo drone," in *Proc. IEEE/RSJ Int. Conf. Intell. Robots Syst.*, 2017, pp. 6855–6862.

[21] C. J. Salaan, K. Tadakuma, Y. Okada, E. Takane, K. Ohno, and S. Tadokoro, "UAV with two passive rotating hemispherical shells for physical interaction and power tethering in a complex environment," in *Proc. IEEE Int. Conf. Robot. Autom.*, 2017, pp. 3305–3312.

[22] A. Briod, P. Kornatowski, J.-C. Zufferey, and D. Floreano, "A collision-resilient flying robot," *J. Field Robot.*, vol. 31, no. 4, pp. 496–509, 2014.

[23] N. Zhao, Y. Luo, H. Deng, and Y. Shen, "The deformable quad-rotor: Design, kinematics and dynamics characterization, and flight performance validation," in *Proc. IEEE/RSJ Int. Conf. Intell. Robots Syst.*, 2017, pp. 2391–2396.

[24] D. Falanga, K. Kleber, S. Mintchev, D. Floreano, and D. Scaramuzza, "The foldable drone: A morphing quadrotor that can squeeze and fly," *IEEE Robot. Autom. Lett.*, vol. 4, no. 2, pp. 209–216, Apr. 2019.

[25] S. Mintchev, S. de Rivaz, and D. Floreano, "Insect-inspired mechanical resilience for multicopters," *IEEE Robot. Autom. Lett.*, vol. 2, no. 3, pp. 1248–1255, Jul. 2017.

[26] J. Shu and P. Chirarattananon, "A quadrotor with an origami-inspired protective mechanism," *IEEE Robot. Autom. Lett.*, vol. 4, no. 4, pp. 3820–3827, Oct. 2019.

[27] P. Sareh, P. Chermprayong, M. Emmanuelli, H. Nadeem, and M. Kovac, "Rotorigami: A rotary origami protective system for robotic rotorcraft," *Sci. Robot.*, vol. 3, no. 22, 2018, Art. no. eaah5228.

[28] Z. Liu and K. Karydis, "Toward impact-resilient quadrotor design, collision characterization and recovery control to sustain flight after collisions," in *Proc. IEEE Int. Conf. Robot. Autom.*, 2021, pp. 183–189.

[29] R. Goldstein, "Self-folding propeller," U.S. Patent 2018/0 257 769A1, Sep. 2018.

[30] O. D. Dantsker, M. Caccamo, R. W. Deters, and M. S. Selig, "Performance testing of aero-naut CAM folding propellers," *in Proc. AIAA Aviation 2020 Forum*, 2020, vol. 1, pp. 1–52.

[31] J. Jang, K. Cho, and G.-H. Yang, "Design and experimental study of dragonfly-inspired flexible blade to improve safety of drones," *IEEE Robot. Autom. Lett.*, vol. 4, no. 4, pp. 4200–4207, Oct. 2019.

[32] *APC 14x4.7 Slow Flyer Propeller LP14047SF*, Nexus Modelling Supplies, Northampton, U.K. Accessed: May 21, 2022. [Online]. Available: https://www.nexusmodels.co.uk/apc-14x4-7-slow-flyer-propeller-lp14047sf.html

[33] A. Mokhtari and A. Benallegue, "Dynamic feedback controller of Euler angles and wind parameters estimation for a quadrotor unmanned aerial vehicle," in *Proc. IEEE Int. Conf. Robot. Autom.*, 2004, vol. 3, pp. 2359–2366.

[34] H. Huang, G. M. Hoffmann, S. L. Waslander, and C. J. Tomlin, "Aerodynamics and control of autonomous quadrotor helicopters in aggressive maneuvering," in *Proc. IEEE Int. Conf. Robot. Autom.*, 2009, pp. 3277–3282.

[35] H.-N. Nguyen and D. Lee, "Hybrid force/motion control and internal dynamics of quadrotors for tool operation," in *Proc. IEEE/RSJ Int. Conf. Intell. Robots Syst.*, 2013, pp. 3458–3464.

[36] W. Craig, D. Yeo, and D. A. Paley, "Geometric attitude and position control of a quadrotor in wind," *J. Guid., Control, Dyn.*, vol. 43, no. 5, pp. 870–883, 2020.

[37] T. Tomić, C. Ott, and S. Haddadin, "External wrench estimation, collision detection, and reflex reaction for flying robots," *IEEE Trans. Robot.*, vol. 33, no. 6, pp. 1467–1482, Dec. 2017.

[38] J. Carlton, *Marine Propellers and Propulsion*, 3rd ed. Oxford, U.K.: Butterworth-Heinemann, 2012.

[39] E. Branlard, *Wind Turbine Aerodynamics and Vorticity-Based Methods: Fundamentals and Recent Applications* (ser. Research Topics in Wind Energy), vol. 7. Berlin, Germany: Springer, 2017.

[40] S. Abrate, *2—Dynamic Behavior of Composite Marine Propeller Blades*, V. Lopresto, A. Langella, and S. Abrate, Eds. Sawston, U.K.: Woodhead Publishing, 2017.

[41] M. H. Dickinson, F.-O. Lehmann, and S. P. Sane, "Wing rotation and the aerodynamic basis of insect flight," *Science*, vol. 284, no. 5422, pp. 1954–1960, 1999.

[42] R. Younes, A. Hallal, F. Fardoun, and F. Hajj, "Comparative review study on elastic properties modeling for unidirectional composite materials," in *Composites and Their Properties*, N. Hu, Ed. Rijeka, Croatia: InTech, Aug. 2012, pp. 391–408.

[43] F. P. Beer, J. E. R. Johnston, J. T. DeWolf, and D. F. Mazurek, *Mechanics of Materials*, 7th ed. New York, NY, USA: McGraw-Hill Education, Jan. 2015.

[44] G. E. Maddux, L. A. Vorst, J. F. Giessler, and T. Moritz, "Stress analysis manual," U.S. Dept. Commerce, Washington, DC, USA, Tech. Rep. AFFDL-TR-69-42, 1969.

[45] J. Anderson, *Fundamentals of Aerodynamics*, vol. 5. New York, NY, USA: McGraw-Hill, 2013.

[46] K. M. Lynch and F. C. Park, *Modern Robotics: Mechanics, Planning, and Control*, 1st ed. New York, NY, USA: Cambridge Univ. Press, 2017.

[47] M. A. Fischler and R. C. Bolles, "Random sample consensus: A paradigm for model fitting with applications to image analysis and automated cartography," *Commun. ACM*, vol. 24, no. 6, pp. 381–395, Jun. 1981.

[48] M. Quigleyet al., "ROS: An open-source robot operating system," in *Proc. ICRA Workshop Open Source Softw.*, 2009, pp. 1–6.

[49] J. Cleland-Huang and A. Agrawal, "Human-drone interactions with semi-autonomous cohorts of collaborating drones," in *Proc. CEUR Workshop*, 2020, vol. 2617, pp. 1–6.

[50] K. Yamaguchi, G. Kato, Y. Kuroda, K. Kiyokawa, and H. Takemura, "A non-grounded and encountered-type haptic display using a drone," in *Proc. Symp. Spatial User Interact.*, 2016, pp. 43–46.

Son Tien Bui (Student Member, IEEE) received the B.Eng. and M.S. degrees in manufacture engineering from the Hanoi University of Science and Technology, Hanoi, Vietnam, in 2009 and 2012, respectively. He is currently working toward the Ph.D. degree in soft robotics with the Soft Haptics Lab, Japan Advanced Institute of Science and Technology, Nomi, Japan, under support from Japan.s Ministry of Education, Culture, Sports, Science and Technology (MEXT) scholarship.

From 2010 to 2018, he was a Lecturer with the Hanoi University of Industry (HaUI), Hanoi. He set up and managed Fablab HaUI, Hanoi, an open lab for student research, from 2016 to now. He completed the JASSO scholarship for Research Assistant from the National Institute of Technology, Tsuruoka College, Tsuruoka, Japan, in 2019. His current research interests include bioinspired robots, tactile sensing/perception, and soft robotics.

Quan Khanh Luu (Student Member, IEEE)) received the B.Eng. degree in mechatronics from the Ho Chi Minh City University of Technology, Ho Chi Minh City, Vietnam, in 2018, and the M.S. degree in robotics in 2021 from the Japan Advanced Institute of Science and Technology (JAIST), Nomi, Japan, where he is currently working toward the Ph.D. degree in robotics with the Soft Haptics Lab.

His current research interests include robot learning and control, tactile sensing/perception, and applications for human–robot interaction.

Mr. Luu was honored as the Best Graduate Student for the outstanding academic performance during his master's degree.

Dinh Quang Nguyen (Member, IEEE) received the Engineer and Master of Science degrees in mechanical engineering from the Hanoi University of Science and Technology, Hanoi, Vietnam, in 2011 and 2013, respectively, and the Ph.D. in materials science degree from the School of Materials Science, Japan Institute of Science and Technology, Nomi, Japan, in 2022 (supported by MEXT Scholarship).

From 2013 to 2018, he was a Lecturer with the Hanoi University of Industry (HaUI), Hanoi. He currently leads a laboratory on Simulation and High-Performance Computing with the Institute of Technology, HaUI. His research interests include soft robotics, biomimetics, functional materials, and mechanical engineering.

Nhat Dinh Minh Le received the B.Eng. degree in mechatronics from the Da Nang University of Science and Technology, Da Nang, Vietnam, in 2019, and the M.S. degree in robotics from the Japan Advanced Institute of Science and Technology (JAIST), Nomi, Japan, in 2021. He is currently working toward the Ph.D. degree in robotics with JAIST under support from doctoral research fellow (DRF) scholarship.

His current research interests include tactile sensing, swarm robotics, and soft robotics.

Giuseppe Loianno (Member, IEEE) received the B.Sc. (Hons.) and M.Sc. (Hons.) degrees in automation engineering from the University of Naples Federico II, Naples, Italy, in 2007 and 2010, respectively, and the Ph.D. degree in computer and control engineering focusing in robotics from the University of Naples Federico II in 2014.

He is currently an Assistant Professor with the New York University, Brooklyn, NY, USA, where he is also the Director of the Agile Robotics and Perception Lab (https://wp.nyu.edu/arpl/) working on autonomous micro aerial vehicles. Prior to this, he was a Lecturer, Research Scientist, and Team Leader with the General Robotics, Automation, Sensing and Perception Laboratory, University of Pennsylvania, Philadelphia, PA, USA. He has authored or coauthored more than 70 conference papers, journal papers, and book chapters. His work has been featured in a large number of renowned international news and magazines. His research interests include perception, learning, and control for agile autonomy of single and multiple microaerial vehicles.

Dr. Loianno received the National Science Foundation CAREER Award in 2022. He is also the recipient of the Conference Editorial Board Best Associate Editor Award at 2022 International Conference on Robotics and Automation (ICRA), the Conference Editorial Board Best Reviewer Award at ICRA 2016, and the National Italian American Foundation Young Investigator Award 2018. He was the Program Chair of 2019 IEEE International Symposium on Safety, Security, and Rescue Robotics (SSRR) and SSRR 2020 as well as the General Chair of SSRR 2022. He has organized multiple workshops on Micro Aerial Vehicles during IEEE/RSJ International Conference on Intelligent Robots and Systems and created the new International Symposium on Aerial Robotics.

Van Anh Ho (Senior Member, IEEE) received the bachelor's degree in electrical engineering from the Hanoi University of Science and Technology, Hanoi, Vietnam, in 2007, and the master's degree in mechanical engineering and the Ph.D. degree in robotics from Ritsumeikan University, Kyoto, Japan, in 2009 and 2012, respectively.

He was a Japan Society for the Promotion of Science (JSPS) Postdoctoral Fellow in 2013 before joining the Advanced Research Center, Mitsubishi Electric Corp., Tokyo, Japan, as a Research Scientist. From 2015 to 2017, he was an Assistant Professor with Ryukoku University, Kyoto, where he led a laboratory on soft haptics, soft modeling. In 2017, he joined the Japan Advanced Institute of Science and Technology, Nomi, Japan, for setting up a laboratory on soft robotics. His current research interests include soft robotics, soft haptic interaction, tactile sensing, grasping and manipulation, and bioinspired robots.

Dr. Ho was the recipient of the prestigious JSPS Research Fellowship for Young Scientist for his Ph.D. course (DC2) and Postdoctoral Fellowship. He was the recipient of the 2019 IEEE Nagoya Chapter Young Researcher Award, the Best Paper Finalists at 2016 IEEE/SICE International Symposium on System Integration (SII) and 2020 IEEE International Conference on Soft Robotics (RoboSoft). He is a Member of the Robotics Society of Japan. He is an Associate Editor for many international conferences, such as IEEE/RSJ International Conference on Intelligent Robots and Systems, SII, RoboSoft, and for journals such as IEEE TRANSACTIONS FOR ROBOTICS, IEEE ROBOTICS AND AUTOMATION LETTERS, and *Advanced Robotics*. He is a General Co-Chair of 2023 SII.